Title
Dominant Controls of Downdip Afterslip and Viscous Relaxation on the Postseismic Displacements Following the Mw7.9 Gorkha, Nepal, Earthquake

Journal
Journal of Geophysical Research: Solid Earth, 122(10)

ISSN
2169-9313

Authors
Zhao, Bin
Bürgmann, Roland
Wang, Dongzhen
et al.

Publication Date
2017-10-01

DOI
10.1002/2017jb014366

Peer reviewed

Dominant Controls of Downdip Afterslip and Viscous Relaxation on the Postseismic Displacements Following the M_w7.9 Gorkha, Nepal, Earthquake

Bin Zhao[1,2], Roland Bürgmann[3], Dongzhen Wang[1,2], Kai Tan[1,2], Ruilin Du[1,2], and Rui Zhang[4]

[1] Institute of Seismology, China Earthquake Administration, Wuhan, China,[2] Key Laboratory of Earthquake Geodesy, Institute of Seismology, China Earthquake Administration, Wuhan, China, [3]Department of Earth and Planetary Science, University of California, Berkeley, CA, USA,[4]National Earthquake Infrastructure Service, Beijing, China

Abstract

We analyze three-dimensional GPS coordinate time series from continuously operating stations in Nepal and South Tibet and calculate the initial 1 year postseismic displacements. We first investigate models of poroelastic rebound, afterslip, and viscoelastic relaxation individually and then attempt to resolve the trade-offs between their contributions by evaluating the misfit between observed and simulated displacements. We compare kinematic inversions for distributed afterslip with stress-driven afterslip models. The modeling results show that no single mechanism satisfactorily explains near- and far-field postseismic deformation following the Gorkha earthquake. When considering contributions from all three mechanisms, we favor a combination of viscoelastic relaxation and afterslip alone, as poroelastic rebound always worsens the misfit. The combined model does not improve the data misfit significantly, but the inverted afterslip distribution is more physically plausible. The inverted afterslip favors slip within the brittle-ductile transition zone downdip of the coseismic rupture and fills the small gap between the mainshock and largest aftershock slip zone, releasing only 7% of the coseismic moment. Our preferred model also illuminates the laterally heterogeneous rheological structure between India and the South Tibet. The transient and steady state viscosities of the upper mantle beneath Tibet are constrained to be greater than 10^{18} Pa s and 10^{19} Pa s, whereas the Indian upper mantle has a high viscosity $\geq 10^{20}$ Pa s. The viscosity in the lower crust of southern Tibet shows a clear trade-off with its southward extent and thickness, suggesting an upper bound value of $\sim 8 \times 10^{19}$ Pa s for its steady state viscosity.

1 Introduction

Earthquakes represent sudden natural rock mechanics experiments that can be used to verify rheological properties of rocks and faults obtained from small-scale laboratory experiments. Numerical modeling of the processes contributing to geodetically observed postseismic deformation helps resolve these properties. Since the early studies of the postseismic deformation following the 1906 San Francisco earthquake (Thatcher, 1983), it has been recognized that transient deformation provides valuable information about viscous rheology beneath the shallow elastic layer of the lithosphere as well

as the mechanics of fault interaction (Bürgmann & Dresen, 2008). Improved knowledge of the mechanical properties of the lithosphere and large-scale faults and of the processes that govern postseismic stress transfer is central to furthering our understanding of the earthquake cycle and seismic hazard.

A large number of earthquakes, including continental events and subduction ruptures, have been explored to gain understanding of the mechanisms that produce the geodetically observed postseismic transients. In the interior and surrounding regions of the Tibetan Plateau, postseismic deformation following several earthquakes with all three types of fault mechanism has been investigated using interferometric synthetic aperture radar (InSAR) and/or GPS. These events include the 1997 Nima, 2001 Kokoxili, 2005 Kashmir, and 2008 Wenchuan earthquakes, as well as transients from earlier historical earthquakes (Bie et al., 2014; Huang, et al., 2014; Ryder, et al., 2011, 2014, 2010; Wang & Fialko, 2014; Wen et al., 2012). These studies have significantly improved our knowledge about the lithosphere strength and constitutive properties beneath the Tibetan Plateau and help inform the contentious debate of whether the lithosphere beneath Tibet allows for rapid flow in a low-viscosity lower crustal channel (Beaumont et al., 2001; Royden et al., 1997). The results further document strong contrasts in rheological structure between the Sichuan Basin and Tibetan Plateau along the eastern edge of the plateau (Huang et al., 2014) and between the Qaidam Basin and the Tibetan Plateau in the north (Ryder et al., 2011).

On 25 April 2015, the M_w7.9 Gorkha earthquake ruptured the lower section of the locked east central Nepal segment of the Main Himalayan Thrust (MHT) from west to east, leaving the locked upper portion still unruptured (e.g., Avouac et al., 2015; Elliott et al., 2016; Qiu et al., 2016; Wang & Fialko, 2015). Two weeks later, the largest M_w7.3 aftershock ruptured near the eastern end of the rupture zone of the mainshock, leaving a small gap unbroken between the mainshock and aftershock slip zones (Lindsey et al., 2015). These two earthquakes provide an opportunity to investigate the lithospheric rheology across the central Himalaya region and the mechanisms that govern their postseismic deformation, as well as to assess the seismic hazard of this region in the aftermath of this event. Several studies have explored the early postseismic deformation following the Nepal earthquake using GPS and/or InSAR data. All these works relied on afterslip modeling to explain the transient postseismic deformation (Gualandi et al., 2016; Mencin et al., 2016; Sreejith et al., 2016), ignoring the effects from viscous relaxation in the lower crust and upper mantle and potential contributions from poroelastic relaxation in the shallow crust.

In this paper we consider data from continuous GPS stations operating both in Nepal and in the southern Tibetan Plateau to capture the transient three-dimensional surface deformation within the first year following the Gorkha earthquake. We attempt to assess the contributions of multiple candidate postseismic mechanisms, namely, poroelastic rebound, aseismic afterslip, and viscoelastic relaxation, to the observed total surface deformation. Since

contributions from these three primary mechanisms are difficult to separate from one another, we first investigate the pattern of deformation from each individual mechanism and then attempt to resolve the trade-offs between contributions from viscous relaxation, afterslip, and poroelastic rebound by carefully evaluating the misfit between calculations and observations.

2 GPS Data and Transient Postseismic Displacements

2.1 Data Processing Method

A substantial number of GPS stations in Nepal, which include both continuous GPS (CGPS) and survey mode sites, were operating prior to the Gorkha earthquake (e.g., Ader et al., 2012). After this event, more GPS stations have been installed to improve the spatial coverage to capture detailed transient postseismic deformation (Gualandi et al., 2016; Mencin et al., 2016). The raw RINEX data from these stations are shared with the research community through UNAVCO (ftp://data-out.unavco.org). In addition, we also rely on continuous GPS data acquired in South Tibet from the Crustal Movement Observation Network of China (CMONOC) (Li et al., 2012).

We processed the GPS data from stations in Figure 1 using standard procedures from RINEX level data to coordinate time series using the GAMIT/GLOBK processing software (Herring, et al., 2015). For each day, loosely constrained GPS daily solutions containing station coordinates, satellite orbit parameters, and tropospheric delay parameters and their full covariances were produced. In this procedure, models of absolute antenna phase center offsets, ocean tidal loading, and pole tide and solid earth tide displacements were applied. Then, a sequential Kalman filter method was employed to combine regional loosely constrained solutions with global solutions obtained from SOPAC (http://sopac.ucsd.edu) using the GLOBK software. Finally, combined daily, loosely constrained solutions were aligned with the International Terrestrial Reference Frame 2008 (ITRF2008) using generalized constraints through approximately 50 global distributed International GNSS (Global Navigation Satellite Systems) Service stations (Altamimi et al., 2011).

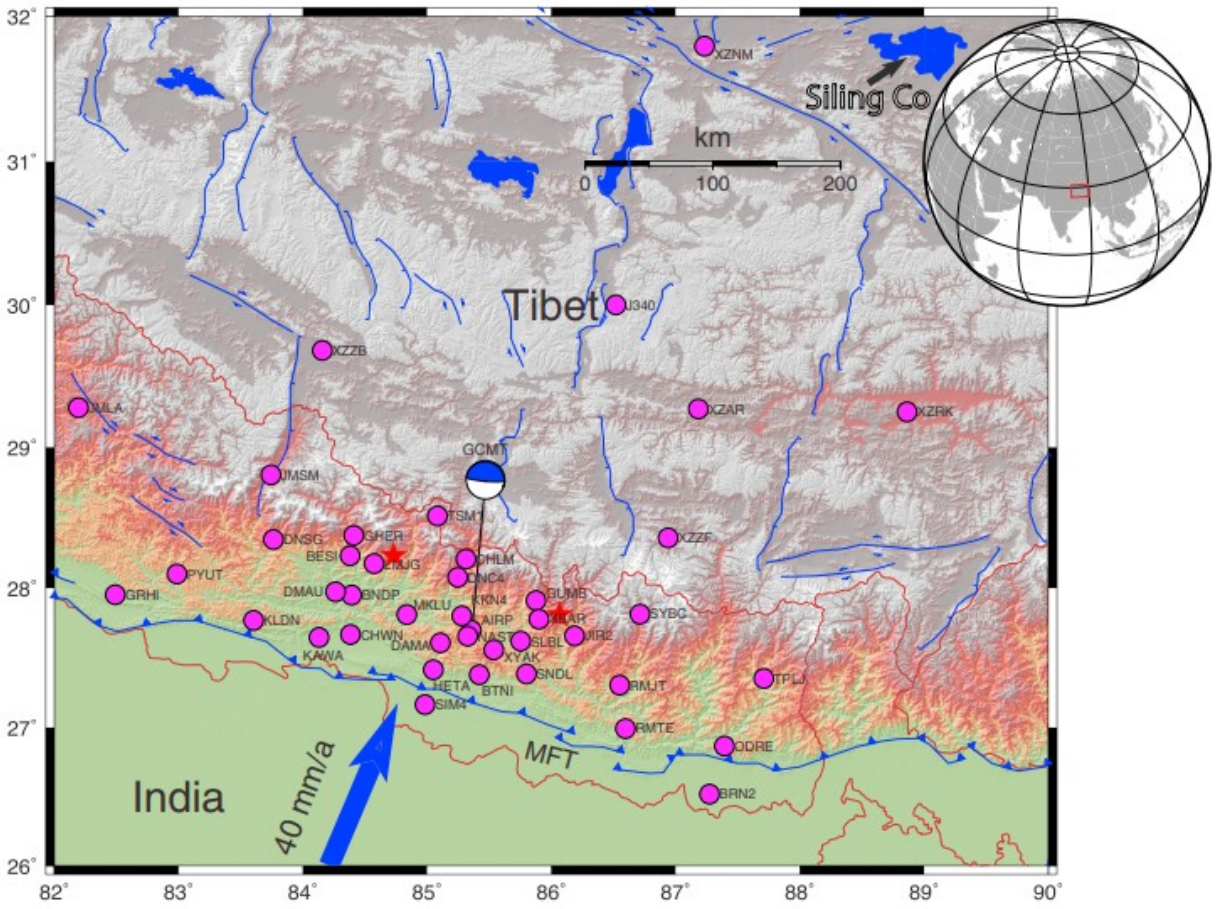

Figure 1

Tectonic context of central Nepal and South Tibet. Active faults illustrated in blue lines are from Taylor and Yin (2009). The red stars are epicenters of the 25 April 2015 mainshock and 12 May 2015 aftershock from U.S. Geological Survey. The blue beach ball shows the mainshock focal mechanism from GCMT. The blue arrow shows the velocity of the Indian Plate relative to Eurasia. Continuous GPS stations used in this study are denoted with magenta circles.

The raw position time series obtained as described above are the sum of (1) a long-term linear velocity representing secular motion in the ITRF2008 frame, (2) seasonal variations due to surface hydrological loading displacements and other annually varying processes, (3) coseismic offsets (including the M_w7.3 aftershock) and/or offsets caused by equipment changes, and (4) transient postseismic deformation due to different postseismic mechanisms. We estimate all nonpostseismic deformations mentioned above at all stations separately and then subtract them one by one from the raw data to isolate the transient postseismic time series. We first subtract coseismic offsets, which were estimated by analyzing position time series 3 days prior and after the mainshock and the largest aftershock (Zhao, Du, et al., 2015).

2.2 Long-Term Velocities

We interpolate the secular linear velocity in the ITRF2008 frame at each site based on an integrated preearthquake velocity field compiled with recently published velocities (Ader et al., 2012; Zhao, Huang et al., 2015). Ader et al. (2012) provide an updated version of secular motions in the Nepal Himalaya region. Their results densely cover the Nepal region; however, there are only few stations in the southern Tibetan Plateau. Zhao, Huang, et al. (2015) published a new velocity field of the CMONOC network spanning 2009 to 2014, including a large number of stations in South Tibet. The respective velocity fields were put into a common reference frame through translations and rotations following Mazzotti et al. (2002). Uncertainties in GPS velocities vary from site to site, and standard errors may not adequately reflect realistic uncertainties from all sources. To make sure that the common stations in the two solutions contribute equal weights in the transformation, we scale the uncertainties of velocities from Zhao, Huang, et al. (2015) by a factor of 2. An improved strain analysis method based on Shen et al., (1996) is then used to interpolate velocities at each site based on the integrated spatially dense velocities. At a given station, a uniform strain rate is assumed and a least squares algorism is utilized to estimate the station velocity solutions as well as strain rate terms and rotation rate. The interpolated secular velocity field agrees well with the observed motions, yielding a small weighted root-mean-square (WRMS) misfit of 0.7 mm/a. Considering velocity uncertainties generally range from 1.0 to 2.0 mm/a in the region, the accumulated displacement due to any velocity bias does not exceed 2.0 mm within 1 year, which is negligible compared to the observed transient postseismic deformation.

2.3 Seasonal Deformation Due To Hydrological Loading

GPS position time series in Nepal and in the southern Tibetan Plateau suffer from strong seasonal variations due to hydrological loading, especially in the vertical and north components (e.g., Bettinelli et al., 2008; Chanard et al., 2014; Fu & Freymueller, 2012). The annual peak-to-peak amplitudes of the loading deformation in the vertical components can reach 20 mm, which is well recorded both by CGPS and Gravity Recovery and Climate Experiment (GRACE) data. Such large oscillations in position could substantially bias the transient vertical displacements especially for stations covering a short time interval. Given that the seasonal displacements in the horizontal component (peak-to-peak amplitudes in the north component of up to 3 mm) are small compared to their postseismic displacements, we only correct the seasonal displacements in the vertical components and seasonal signals in the horizontal components at GUMB and NAST, which show relatively large fluctuations. Monthly GRACE Level-2 solutions from 2002 to 2016 provided by Jet Propulsion Laboratory were processed following a similar procedure described by van Dam, et al. (2007) to obtain equivalent water height time series. The annual and semiannual terms were estimated by analyzing the GRACE-derived position data. We validate our seasonal corrections by comparing to updated seasonal components of Fu and Freymueller (Y. Fu,

personal communication, 2017) and find that the difference between these respective corrections is very small compared to the eventually calculated vertical postseismic deformation. We also evaluate the GRACE-derived seasonal amplitudes and phases by comparing with the GPS-derived results at several sites and find the differences are too small to bias the final postseismic motions. Finally, the annual and semiannual correction terms are applied to all GPS time series. As an example, Figure S1 in the supporting information shows the vertical position time series before and after removing seasonal variations at CHLM station in north Nepal.

2.4 Transient Postseismic Deformation

For the purpose of calculating the initial 1 year cumulative postseismic displacements and their uncertainties, it is convenient to parameterize the time-dependent postseismic deformation using the logarithmic term in equation 1 (e.g., Freed, et al., 2010).

$$u(t) = a_1 + a_2 \ln\left(1 + \frac{t - t_0}{\tau}\right), \quad (1)$$

where $u(t)$ is the transient GPS time series after removing offsets, secular velocities, and seasonal components (Figure S2), a_1 is a constant, and a_2 is the postseismic amplitude. The logarithmic relaxation time (τ) describes the decay of postseismic deformation, and t is the GPS observation epoch after the time of the mainshock t_0. We consider decay constants over a range of values to estimate other model parameters and resolve the trade-off between τ and the misfit to the displacement time series. Through trial and error, we find that the τvalue is relatively insensitive to the final result over a wide range from 10 to 300 days and a uniform τ value of 30 days allows us to fit all the transient time series well. Therefore, we assign a uniform τ of 30 days to estimate the postseismic amplitude a_2 and calculate the accumulated postseismic deformation during the first year following the mainshock. One sigma uncertainties of cumulative displacements are taken as the WRMS of the scatter of the position data about the prediction from equation 1. The average uncertainty is 2.0 mm in the horizontal component and is 6.5 mm in the vertical component.

Figure 2 shows the accumulated horizontal and vertical postseismic displacements within 1 year of the mainshock (data are available in the supporting information Table S1). The amplitudes and azimuths of the horizontal postseismic motions exhibit a similar pattern as the coseismic offsets. The largest postseismic displacements lie along the northern border between Nepal and China. The maximum horizontal displacement of 7.3 cm occurs at GUMB (Figure 2a). Almost all stations record postseismic uplift except for AIRP, JMLA, and KKN4. As the records of AIRP and JMLA station only cover 45 and 71 days, their vertical displacements are not reliable. Although the geologic setting of KKN4 is documented as bedrock (Gualandi et al., 2016), it is probably affected by rapid groundwater depletion in Kathmandu. The nearby station NAST suffered from rapid subsidence with a

rate of approximately −112 mm/a prior to the mainshock, demonstrating rapid land subsidence due to water pumping in the Kathmandu Basin. Thus, we exclude AIRP and the vertical components at KKN4 and JMLA in the following modeling.

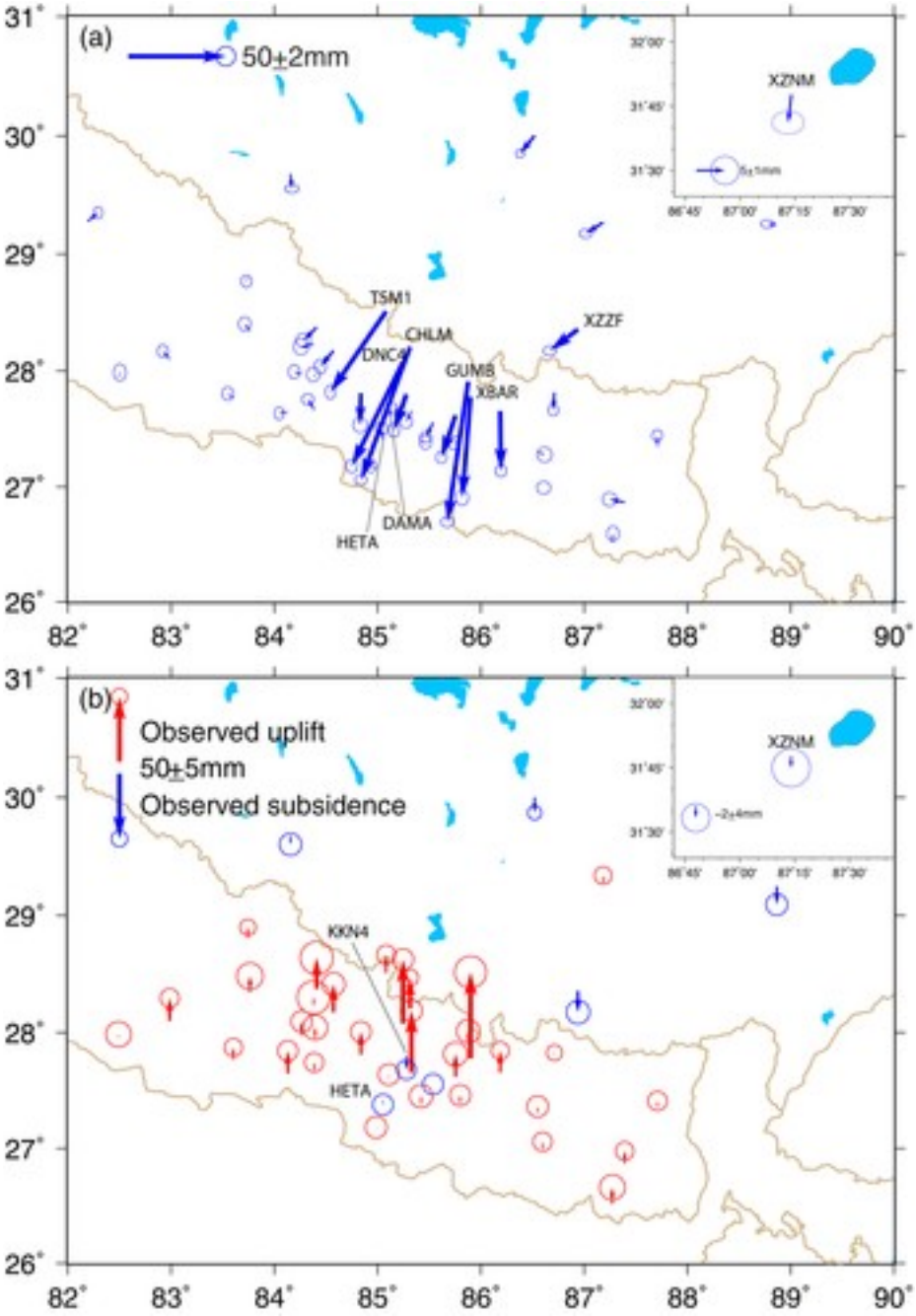

Figure 2

GPS observed total (a) horizontal and (b) vertical displacements within first year of the Gorkha earthquake with 95% confidence level error ellipses. Insets show the far-field displacements at station XZNM, which is located more than 500 km from the rupture (Figure 1).

3 Modeling Methods

The objective of the paper is to determine the mechanical processes that control the observed GPS postseismic deformation after the 2015 Gorkha, Nepal, earthquake. Three primary mechanisms are thought to be responsible for transient postseismic deformation, namely, poroelastic rebound in the shallow crust, aseismic afterslip surrounding the coseismic rupture areas, and viscoelastic relaxation in the lower crust and upper mantle. Here we present brief descriptions of the methods used to model these different mechanisms.

3.1 Poroelastic Rebound Model

Coseismic stress changes induced by an earthquake rupture alter the pore-pressure gradients in the surrounding rocks. Flow of fluids in the crust gradually restores hydrostatic equilibrium. This process of fluid-pressure reequilibration leads to deformation of the Earth medium and causes deformation at the surface that can be recorded by geodetic instruments or water level changes in wells (Jonssón et al., 2003; Peltzer et al., 1996, 1998). Deformation from poroelastic rebound can be estimated by the difference between two coseismic displacement fields predicted using undrained and drained values of the Poisson's ratio in elastic dislocation models. This method has been widely applied to investigate the contributions from the poroelastic response following earthquakes.

In addition to the traditional approach of calculating the fully relaxed poroelastic response, Wang and Kümpel (2003) developed a method to model time-dependent poroelastic rebound processes induced by earthquakes or pumping in a multilayered half-space. In forward models, Green's functions are generated based on a first-order multilayered elastic structure (V_p, V_s, and density) and depth-dependent hydraulic diffusivity (Figure 3a), and then the coseismic rupture model is used to calculate time-dependent poroelastic relaxation caused by the Gorkha earthquake.

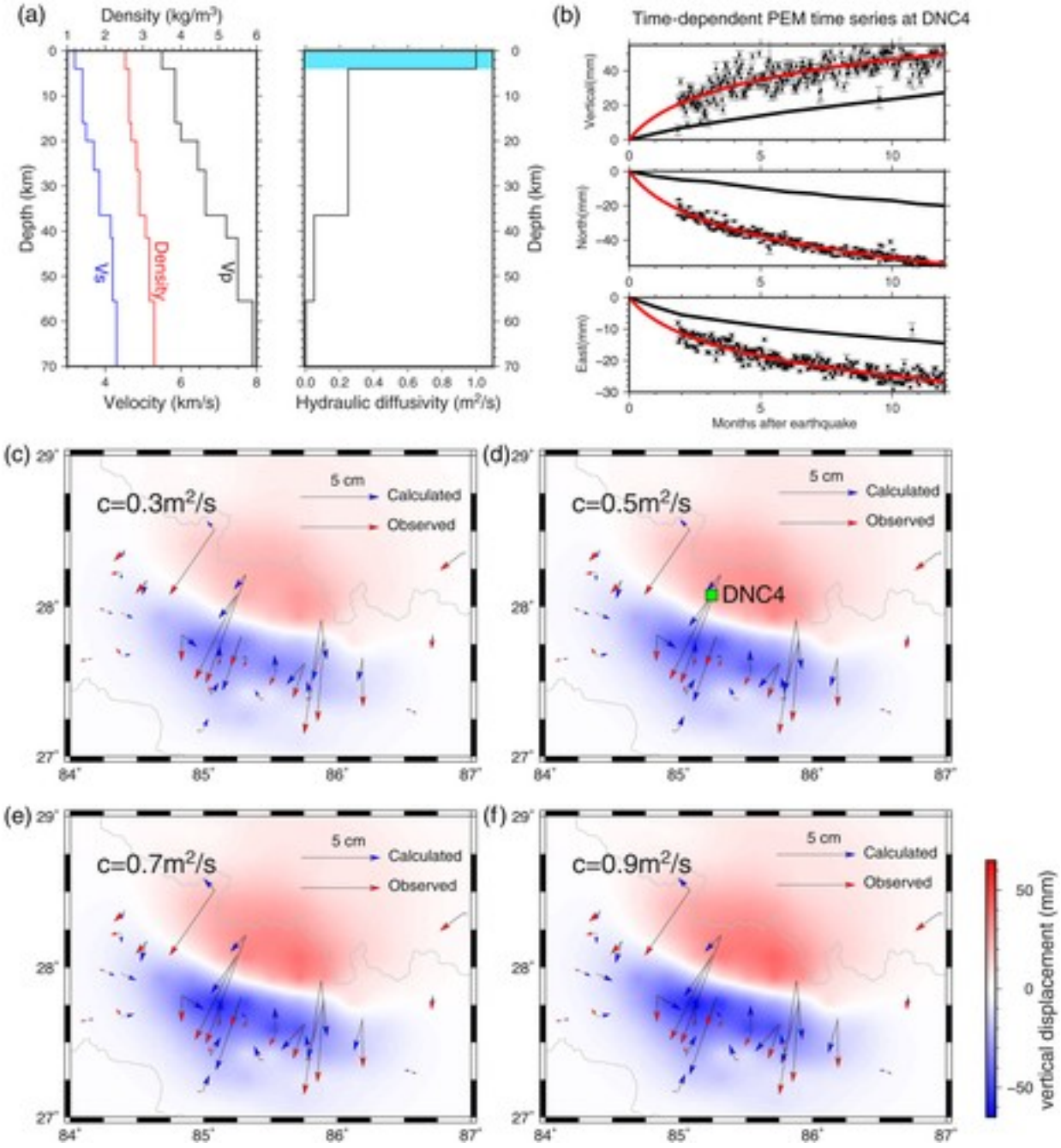

Figure 3

(a) Multilayered earth structure used in the study of time-dependent poroelastic rebound displacements. The 1-D velocity model is the same as in Avouac et al. (2015), and hydraulic diffusivity, *c*, in the uppermost 4 km (light blue region) is varied from 0.1 to 1.0 m^2/s. (c–f) Comparison of GPS observed initial 1 year postseismic displacements and poroelastic rebound displacements with different hydraulic diffusivity values of 0.3, 0.5, 0.7, and 0.9 m^2/s in the multilayered earth structure (Figure 3a). (b) Observed (black dots with error bars) and best fit modeled (red line) time series from equation 1, as well as time-dependent poroelastic rebound displacements (black line) with a hydraulic diffusivity of 0.5 m^2/s at northern Nepal station DNC4, which is labeled in (Figure 3d).

3.2 Kinematic Afterslip Model

Afterslip is the process by which coseismic stress changes cause aseismic slip following an earthquake (e.g., Marone, et al., 1991). Such aseismic slip can occur both updip and downdip of the rupture surface on the sections of the fault that have velocity-strengthening properties. The afterslip distribution on the rupture fault surface can be explored by inverting the GPS-measured cumulative postseismic displacements. We assume that the afterslip can be described by a dislocation model of distributed slip in an elastic half-space (Okada, 1992). We minimize the objective function:

$$F(s,\beta) = \|W(Gs - d)\| + \beta\|\nabla^2 s\| \quad (2)$$

where s represents the estimated slip components, W is the diagonal weight matrix constructed from the observation uncertainties, d is the geodetic data vector, G is the matrix of Green's functions, ∇^2 is the finite difference of the Laplacian operator used to smooth the slip model, and β is a factor used to adjust smoothness. The optimal model solution, s, is obtained by using the bounded variable least squares algorithm (Stark & Parker, 1995), with the optimal value of β to be determined for the trade-off between the model roughness and data misfit.

The fault is assumed to be planar, and its dip angle is adjusted to 7° by trial and error (Figure S3), which agrees well with preferred dip angles used in several published coseismic slip models (e.g., Avouac et al., 2015; Wang & Fialko, 2015). The top of the fault is buried 3 km beneath the surface. The length of the rupture surface is extended to 265 km, and the downdip width of the fault is assigned to 200 km. The fault plane is divided into 30 by 30 small patches with a patch size of 8.83 km × 6.67 km in the strike and dip directions. Each individual dislocation patch is allowed to slip only by thrusting in the dip direction given that coseismic shear-stress changes in the strike direction are negligible. In the afterslip inversions we add another constraint of zero slip in the region of peak coseismic slip (>2 m) (Tan et al., 2016).

3.3 Stress-Driven Afterslip Model

The kinematic slip inversions from geodetic observations are not controlled by constitutive properties of fault interfaces. Although the kinematic results can be used to explore the first-order source of the postseismic deformation, it is not clear whether the results represent physically plausible patterns of slip. In some cases, the kinematic afterslip models can yield unexpected slip far away from the base of the coseismic fault plane and peak coseismic stress changes (e.g., Freed et al., 2006; Huang et al., 2014).

Stress-driven frictional or frictionless afterslip models (Barbot, et al., 2009; Freed et al., 2006; Huang et al., 2014; Johnson, et al., 2006; Perfettini & Avouac, 2007; Rousset et al., 2012) and viscoelastic thin tabular shear-zone models (Hearn, et al., 2002; Hu, Bürgmann, Uchida, et al., 2016) have been successfully employed to investigate stress-driven afterslip following different events. In this study, the stress-driven afterslip models are

calculated using the boundary element code POLY3D (Thomas, 1993), which calculates the total slip that results when the shear-stress loading from the coseismic rupture (Tan et al., 2016) is fully relieved. For comparison with the kinematic afterslip model, we scale the frictionless afterslip on the fault plane to minimize the data misfit between observed and calculated surface displacements. As the MHT at shallower depths may remain locked during the postseismic period, we calculate models where stress-driven afterslip is only allowed downdip of a line located at some distance from the Main Frontal Thrust (MFT), which we refer to as the locking width. We acknowledge the simplicity of this zero-friction forward model, which has no frictional properties and assumes all of the slip patches have the same time-dependent evolution, and the resulting slip distribution is sensitive to fault geometry and extent of the fault plane.

3.4 Viscoelastic Relaxation Model

We employ the spectral element method code VISCO2.5D to calculate the deformation due to viscoelastic relaxation of coseismic stress changes in the lower crust and upper mantle of Tibet and India. The code can determine the three-dimensional quasi-static displacement field from relaxation in an effectively 2-D viscoelastic structure, which is azimuthally symmetric about a prescribed pole (Pollitz, 2014). It first calculates the quasi-static displacements on the Laplace transform domain and then yields transient displacements through an inverse Laplace transformation (Pollitz, 2014). This method has been successfully used to study laterally variable viscoelastic structure and water content in the Southern California mantle by analyzing postseismic deformation following the 1992 M7.3 Landers and 1999 M7.1 Hector Mine, California, earthquakes (Pollitz, 2015).

Coseismic source slip models of the mainshock and the largest aftershock (M_w7.3) are applied as input to calculate viscous relaxation (Tan et al., 2016). The source models of Tan et al. (2016), which were derived from GPS data from South Tibet (Zhao, Du, et al., 2015) and Nepal (Galetzka et al., 2015) and InSAR data (Lindsey et al., 2015), are consistent with various published models (e.g., Avouac et al., 2015; Wang & Fialko, 2015). Once the earthquake rupture source is given, the postseismic deformation on the Earth's surface depends on the rheological structure at depth. Geological and geophysical observations clearly show that the lithospheric structure and mechanical properties of India are very different from those of the southern Tibetan Plateau (Beaumont et al., 2001; Monsalve et al., 2006; Nábělek et al., 2009; Unsworth et al., 2005). In VISCO2.5D we define a first-order rheological structure that reflects the observed lateral variation of the lithospheric structure across central Nepal. As shown in Figure 4, the depth extent of the elastic upper crustal layer in Tibet is initially assigned to 30 km, and the lower crust in southern Tibetan Plateau reaches down to the Moho at 70 km depth, which represents the average crustal thickness of the Tibetan Plateau. The upper mantle of Tibet extends from 70 km down to 200 km depth, below which the stress changes due to the coseismic loading drop to

negligible levels. For the Indian Plate, we assume the thickness of its elastic layer is 50 km, which is within the range of estimates of effective elastic thickness (T_e) of 40–70 km, for North India (Audet & Bürgmann, 2011; Burov & Watts, 2006; Maggi et al., 2000), below which is the viscoelastic upper mantle. The boundary between the lithospheres (different mantle and crustal structure) of India and southern Tibet is initially assigned to be approximately 167 km (1.5°) north from the MFT (model geometry parameter *D* in Figure 4). Seismic velocity and density profiles are used to define the shear modulus in different model volumes of India and South Tibet, respectively (Hetényi et al., 2007; Monsalve et al., 2006). In order to achieve the needed accuracy of the model calculations, the computational grid is densely spaced near the coseismic rupture zone and less dense far from the rupture (Figure 4).

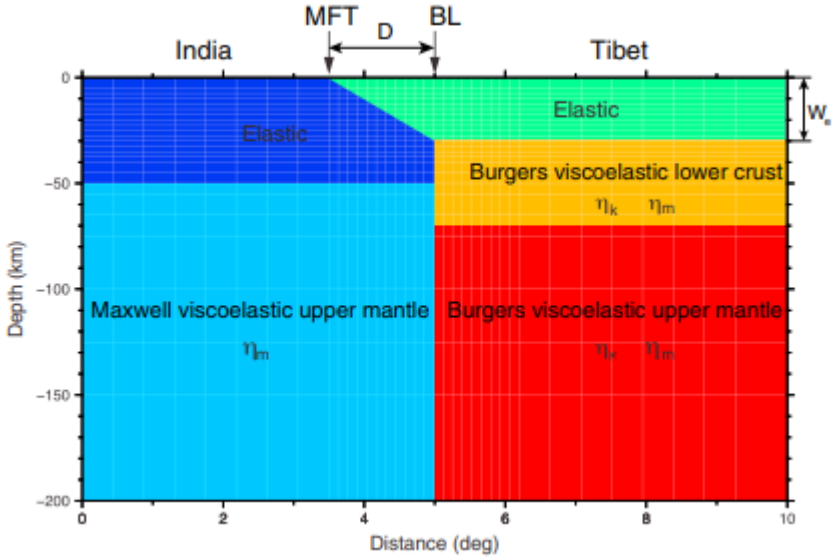

Figure 4

Laterally heterogeneous model rheological structure across the central Nepal Himalaya region. “BL” is defined as the boundary between the lithospheres (different mantle and crustal structure) of India and Tibet. “D” is the distance between BL and the MFT and W_e is the elastic layer thickness in southern Tibet. A Burgers body is used to represent the flow in the lower crust and upper mantle beneath the southern Tibetan Plateau. Maxwell material is used for the upper mantle below India.

We rely on a biviscous Burgers body rheology to represent the viscoelastic relaxation of the lower crust and upper mantle beneath southern Tibet and use a linear Maxwell body for the India upper mantle. The biviscous rheology can capture the apparent rapid decay of effective viscosities in the initial stages of viscoelastic relaxation (Pollitz, 2003; Ryder et al., 2011). The analog for the Burgers body rheology is a Maxwell element in series with a Kelvin element, so its relaxation depends on four parameters: the steady state shear modulus and viscosity (μ_m and η_m) of the Maxwell element and transient shear modulus and viscosity ($\mu_k$and η_k) of the Kelvin element. The viscous relaxation models are assessed by comparison of the calculated time-dependent surface deformation with the GPS observations.

3.5 Multiple-Mechanism Modeling

Models invoking individual postseismic mechanisms often fail to satisfactorily explain the postseismic deformation captured by geodetic observations, and the postseismic deformation following most large earthquakes includes significant contributions by multiple mechanisms. Multiple-mechanism models have been considered for studying postseismic deformation following several earthquake events, such as the 1989 M_w6.9 Loma Prieta earthquake, 2002 M_w7.9 Denali earthquake, 2004 M_w9.2 Sumatra-Andaman earthquake, and 2011 M_w9.0 Tohoku earthquake (Freed et al., 2006; Gunawan et al., 2014; Hu, Bürgmann, Uchida, et al., 2016; Huang, et al., 2016).

After evaluating single-mechanism models invoking poroelastic rebound, afterslip, and viscoelastic relaxation, we carry out a suite of viscous relaxation models varying the viscosity of Tibet's lower crust and the model geometry parameter D (other parameters of rheological structure are fixed), and poroelastic rebound models (PEM) with a range of hydraulic diffusivity values in the upper 4 km of the crust, and remove these contributions from the observations. Then afterslip distributions are inverted from the residual data set using the same method described in section 3.2. We assess these models by the misfit to the observations and by the degree to which the inverted afterslip agrees with the depth distribution of afterslip in the preferred stress-driven afterslip model. We explore the multiple-mechanism models using a simple grid search approach. A schematic flowchart of our procedure for determining the multiple-mechanism models is depicted in Figure 5.

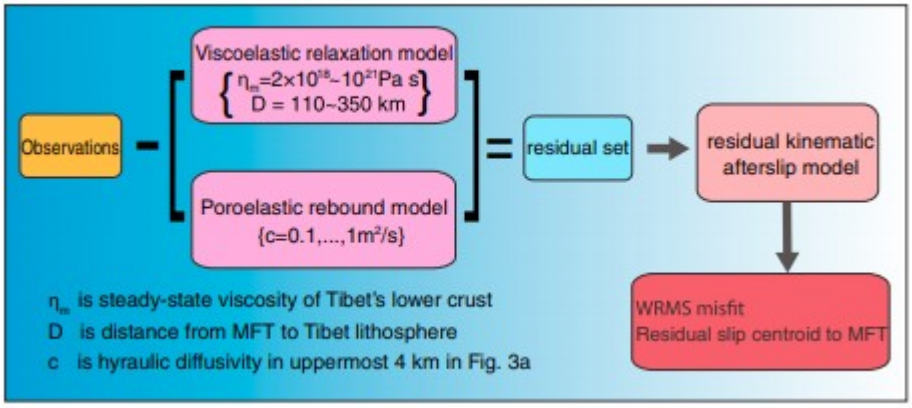

Figure 5

Schematic flowchart of the procedure for solving the multiple-mechanism models.

4 Model Results

4.1 Poroelastic Rebound

The inferred poroelastic rebound depends on multilayered elastic parameters (V_p, V_s, and density) and hydraulic diffusivity (Figure 3a), as well as on the earthquake rupture model. Laboratory studies and field data indicate that

the hydraulic diffusivity decreases rapidly below a few kilometers (Ingebritsen & Manning, 1999); however, knowledge of the hydraulic diffusivity in this region is very limited. We estimate a suite of poroelastic rebound displacements based on a multilayered earth structure shown in Figure 3a, in which the hydraulic diffusivity in the uppermost 4 km (light blue colored zone in Figure 3a) varies from 0.1 to 1.0 m^2/s following Fialko (2004). Three-dimensional poroelastic rebound displacements with hydraulic diffusivity values of 0.3, 0.5, 0.7, and 0.9 m^2/s are illustrated, as well as the observed 1 year horizontal displacements (Figures 3c–3f). The poroelastic rebound models show a clear hinge line that separates subsidence in the south from uplift in the north. The predicted vertical deformation pattern is opposite to that of the coseismic rupture (e.g., Lindsey et al., 2015) and disagrees with that of the observations as shown in Figure 2b. The predicted horizontal motion directions are similar to the GPS observations; however, most of their amplitudes are smaller. Significant horizontal model displacements concentrate within a narrow zone along the hinge line. The time-dependent poroelastic rebound time series at north Nepal station DNC4 using the hydraulic conductivity structure shown in Figure 3a with a representative hydraulic diffusivity of 0.5 m^2/s show that the surface displacements gradually increase within the first few months and then grow slowly (Figure 3b). The WRMS misfits for the poroelastic rebound models range from 12.4 to 13.5 mm (for different hydraulic diffusivities)—a very poor fit compared to other models, implying that the poroelastic rebound model alone cannot explain the GPS observations.

4.2 Kinematic Afterslip Model

The 1 year three-dimensional displacements are used to invert for the distributed afterslip. By examining the trade-off curve between the model roughness and data misfit, we select a smoothing factor of $\beta = 0.08$ for our final solution (Figure 6), which provides a smooth model with minimal increase in misfit. The corresponding afterslip source model with the rupture exclusion constraint is illustrated in Figure 7a, which yields an afterslip pattern, moment release, and data misfit similar to those from the kinematic model without the additional constraint in the coseismic zone (Figure S9a). The maximum slip magnitude is 320 mm. The moment release is estimated to be 1.0×10^{20} Nm when using a depth-dependent rigidity modulus following Table 3 in Gualandi et al. (2016), equivalent to $M_w = 7.33$, approximately 13% of the coseismic moment.

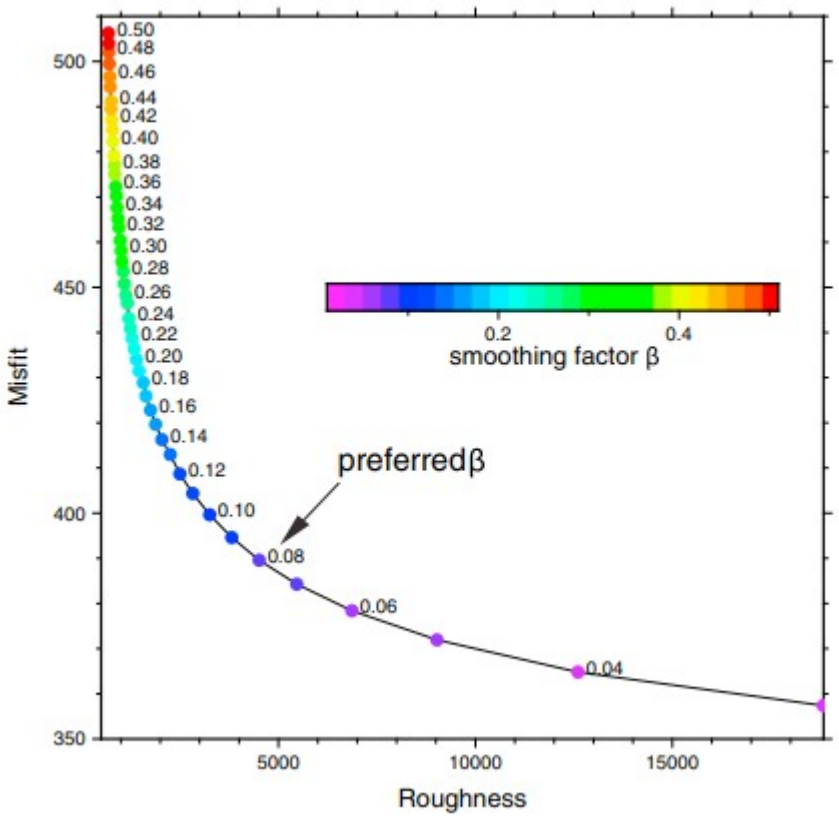

Figure 6

Trade-off curve between model roughness and misfit (weighted residual sum of squares) to the GPS data of the distributed afterslip model, depending on the weight β (indicated by circle colors) put on smoothing in the inversion.

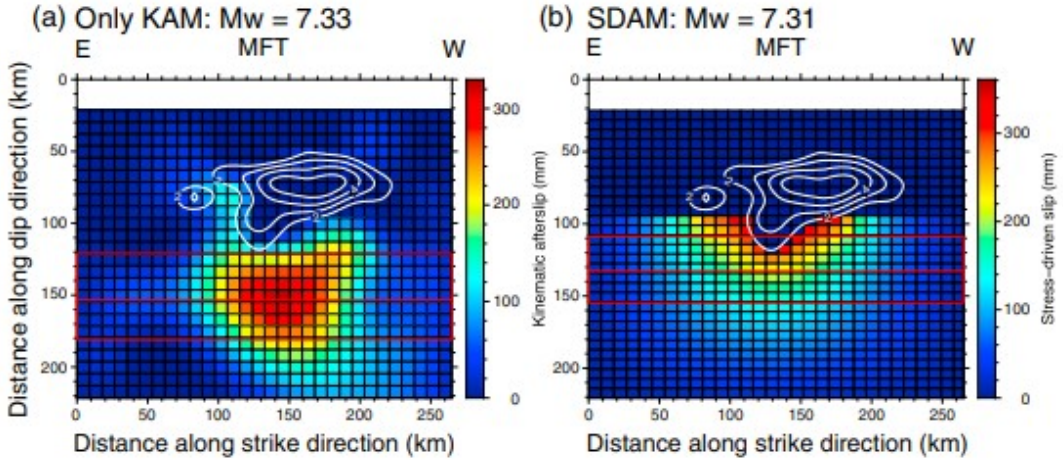

Figure 7

(a) Kinematic afterslip distribution from inversion with the rupture exclusion constraint assuming no contributions from viscous relaxation and (b) stress-driven afterslip distribution in which 17% of total coseismic stress is relieved downdip of a 95 km wide locked MFT to best match the initial 1 year deformation. The shallow portion of the MHT (from surface to 21 km depth) is assumed to be fully locked. White lines depict the mainshock and *M*7.3 aftershock coseismic slip contours with 1 m

intervals (Tan et al., 2016). Red boxes show the distance to the afterslip centroid (the middle lines) and ranges within which 50% of moment is relieved in these two models.

As shown in Figure 8a (zoomed view is shown in Figure S5), the observed horizontal surface displacements are well explained by the downdip afterslip model. The WRMS misfit for this afterslip model is only 4.8 mm, representing a good fit to the data for most stations. Although the agreement between the observed and modeled vertical displacements is not as good as for the horizontal components, especially at stations farther away from the rupture, the model still predicts comparable uplift in north Nepal (Figures 8b and S5b).

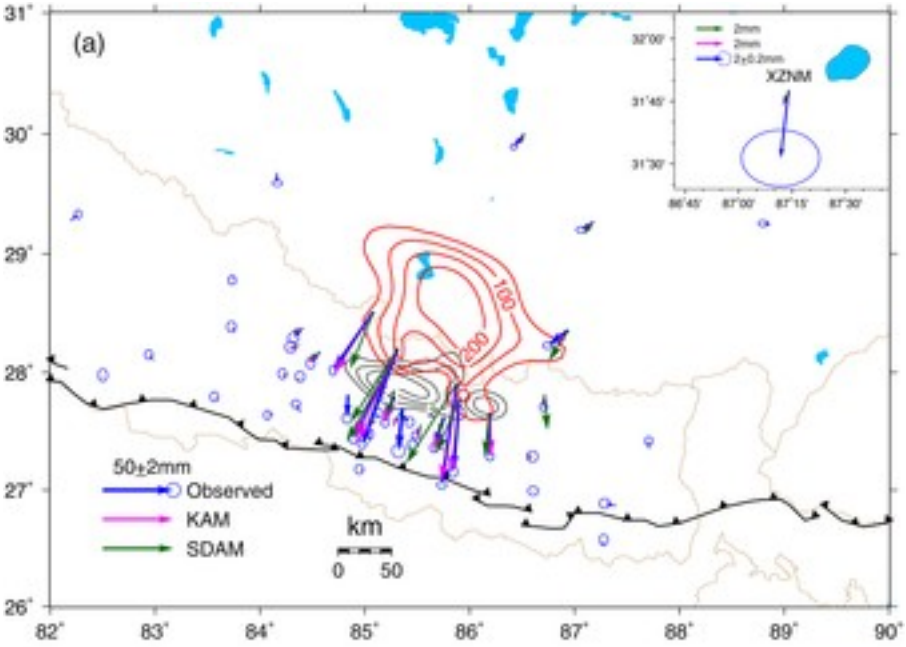

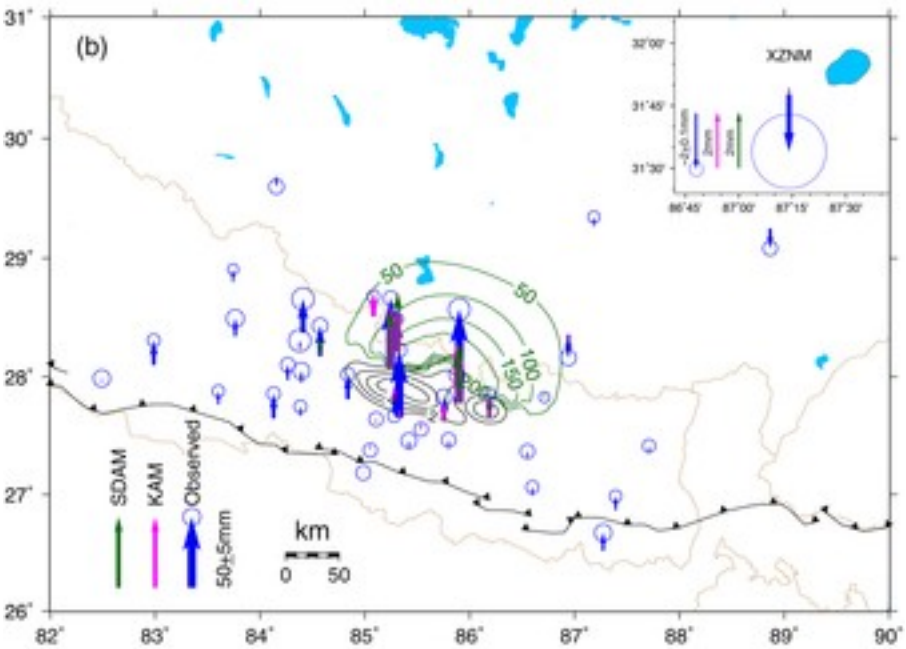

Figure 8

(a) Comparison of GPS observed horizontal displacements and kinematic and stress-driven afterslip models. Inset shows the far-field displacements at XZNM station, which is located more than 500 km from the rupture (Figure 1). (b) Same as Figure 8a but for vertical component. The mainshock and the largest aftershock ruptures are contoured with black lines at 1 m intervals. Red (Figure 8a) and green (Figure 8b) contours at 50 mm intervals represent the slip distribution of the KAM and SDAM models, respectively.

The inferred afterslip primarily concentrates on the downdip extent of the coseismic rupture. Considering the shallow dip angle of the fault plane, we use the slip centroid distance-from-MFT ($W_{\mathrm{MFT}}^{\mathrm{SC}}$, SC stands for slip centroid) to assess whether the kinematic afterslip model is physically reasonable. The $W_{\mathrm{MFT}}^{\mathrm{SC}}$ is 153 km (Figure 7a) for the preferred kinematic afterslip model, compared to 81 km for the coseismic rupture. Our best fit afterslip model favors a very broad distribution and afterslip far downdip of the rupture, which is similar to the results of Gualandi et al. (2016). Checkerboard resolution tests are carried out to examine whether the downdip afterslip is well constrained by the data. The results show that the aseismic slip on the far downdip fault plane under South Tibet is more difficult to recover, suggesting that the inferred distribution of the downdip afterslip is not well resolved (Figure S4).

4.3 Stress-Driven Afterslip Model

The coseismic rupture releases stress on the main asperities and loads the fault away from the coseismic rupture, including the downdip and updip extensions. To model the stress-driven afterslip caused by the coseismic stress changes, we first define the extent of the asperity zone to be within the area where the coseismic slip exceeds a given threshold value (S_t). We investigate four different S_t values, namely, 0.5, 1, 2, and 3 m. Using POLY3D (Thomas, 1993), we compute the afterslip that fully relieves the coseismic shear-stress changes on the frictionless fault plane away from the rupture. To investigate the first-order stress-driven afterslip models, we scale the stress-driven afterslip by multiplying with a uniform ratio (α). The initial stress-driven afterslip model predicts substantial slip around the asperity zones, including the shallow MHT updip of the coseismic rupture, which disagrees with the observed minimal deformation close to the MFT and the distribution found in the preferred kinematic model (Figure 7a). To account for the possibility that the shallow MHT remains locked after the mainshock, we introduce another parameter, W_L, which represents the locking/coupling width from the MFT (along the dip direction). In each case, we perform a grid search of α and W_L to minimize the WRMS misfit between the calculated and observed surface displacements. The minimum WRMS value is achieved when S_t is 2 m, and we hold this value fixed in the following analysis.

Figure 9 shows the grid search result with color-contoured values of WRMS over a range of W_L and α values. There is a clear correlation between these two parameters, in which αdecreases with decreasing W_L. A relatively wide range of W_L (70–110 km) and α (0.12–0.22) can produce stress-driven models

with good agreement with the observations. The best fit stress-driven afterslip model is found for W_L=95 km and α=0.17 (red star in Figure 9 and slip distribution shown in Figure 7b). The preferred locking width from the MFT inferred from the postseismic modeling is close to the average locking-line distance (black line in Figure 9, see data in Table S2) found in recent interseismic planar dislocation models of the interseismic deformation (Bettinelli et al., 2006; Feldl & Bilham, 2006; Jouanne et al., 2004) and the northern edge (~0.8 coupling coefficient contour) of the distributed coupling model of Ader et al. (2012).

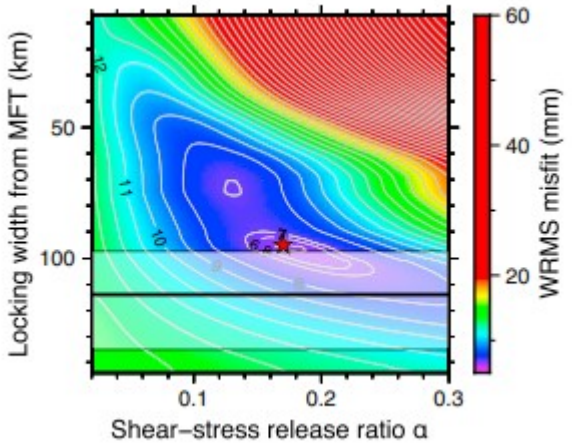

Figure 9

WRMS misfit between observations and a series of stress-driven afterslip models as a function of locking width from the MFT, W_L, and fraction of total release of coseismic shear-stress increase, α. The red star represents the optimal calibrated stress-driven afterslip model with a minimum WRMS of 6.5 mm. The transparent rectangular region shows the range of best fit locking-line distances obtained from models of interseismic Nepal GPS velocities and/or leveling data (Ader et al., 2012; Bettinelli et al., 2006; Feldl & Bilham, 2006; Jouanne et al., 2004) and the horizontal black line shows their average.

The calibrated stress-driven afterslip model depicts the first-order feature of spatial distribution that is physically reasonable given the coseismic stress-change field. The aseismic slip peaks immediately downdip of the rupture and decays gradually from approximately 330 mm to less than 50 mm within 50–70 km from the coseismic rupture (Figure 7b), producing a W_{MFT}^{SC} of ~132 km. The WRMS misfit of the scaled stress-driven model (6.5 mm) is greater than that of the kinematic afterslip inversion (4.8 mm). Based on inspection of the predictions and observations in Figure 8 (zoomed view in Figure S5), the largest discrepancies occur in the northern region of Nepal. This may be due to errors in our coseismic source model driving the afterslip, the simplified geometry and locking line of our model MHT, and contributions of the other postseismic mechanisms. In the future, more complex stress-driven models should be developed to provide constraints on the frictional properties and/or rheology of the deep-seated shear zone.

4.4 Viscoelastic Relaxation

First, we study the individual effects of relaxation in three different rheological domains on the surface deformation, namely, the upper mantle flow beneath India, upper mantle flow beneath Tibet, and lower crustal flow beneath Tibet. In these forward models we do not consider the interaction between relaxation in the different domains, but this provides useful information about the spatial patterns of deformation produced by their relaxation. To this end, we allow viscoelastic relaxation only in one rheological unit, while the other units are defined to be “elastic” (infinite viscosity). We use the domain viscosities from our eventual preferred viscous relaxation model. Viscoelastic relaxation of stresses in the upper mantle beneath Tibet produces relatively small displacements toward Nepal within a broad region of southern Tibet and even less northward motion in central Nepal (Figure S6). The lower crustal flow beneath Tibet results in a more localized zone of southward horizontal motions in southern Tibet and northern central Nepal (Figure S7). Vertical motions from the lower crustal relaxation model are also more localized and opposite in orientation to those found in the upper mantle model. Finally, relaxation in the upper mantle of India predicts only northward motions in central Nepal and produces uplift to the south and subsidence to the north of the northern edge of the mainshock rupture (Figure S8). In the next three sections we describe constraints that allow us to determine optimal viscosity values for each of the three domains in our simple model structure.

4.4.1 Upper Mantle Viscosity Beneath India

Figure 2 shows that GPS observed postseismic deformation consists of predominately southward motion in northern India and southern Tibet. However, stations in southern Nepal observed very small postseismic deformation, and some of them capture modest northward motions of less than ~5 mm (e.g., HETA and DAMA, Figure 2b). We test three steady state Maxwell viscosities, 10^{18}, 10^{19}, and 10^{20} Pa s and find that our models predict large (>5 mm/yr) northward motions at several sites in southern Nepal when η_m^{UMI} is lower than 10^{20} Pa s, which disagrees with the observations. A steady state viscosity of 10^{20} Pa s or larger inferred from our simple tests is also supported by the high effective elastic thickness of the lithosphere, T_e, of 40–70 km for northern India (Audet & Bürgmann, 2011; Burov & Watts, 2006; Maggi et al., 2000).

4.4.2 Upper Mantle Viscosity Beneath Southern Tibet

Both the preferred kinematic and stress-driven afterslip models (inset in Figure 8a) underestimate the far-field southward motion at station XZNM, which is located at least 500 km north from the rupture. Position time series at this station show that the accumulated transient displacement within 1 year is more than 5.0 mm in its north-south component (Figure 10), whereas the prediction from the afterslip model is 1.6 mm or less. Similarly, relaxation in the lower crust beneath Tibet, with viscosities that predict displacements comparable to those observed in southern Tibet and northern

Nepal, produces less than 1 mm offset at this station (Figure S7), and we also find negligible motion at XZNM from relaxation in the India mantle (Figure S8). Thus, the postseismic deformation in this far-field location can be predominantly attributed to relaxation in the upper mantle beneath Tibet, and we constrain the Tibet mantle viscosity using the XZNM time series.

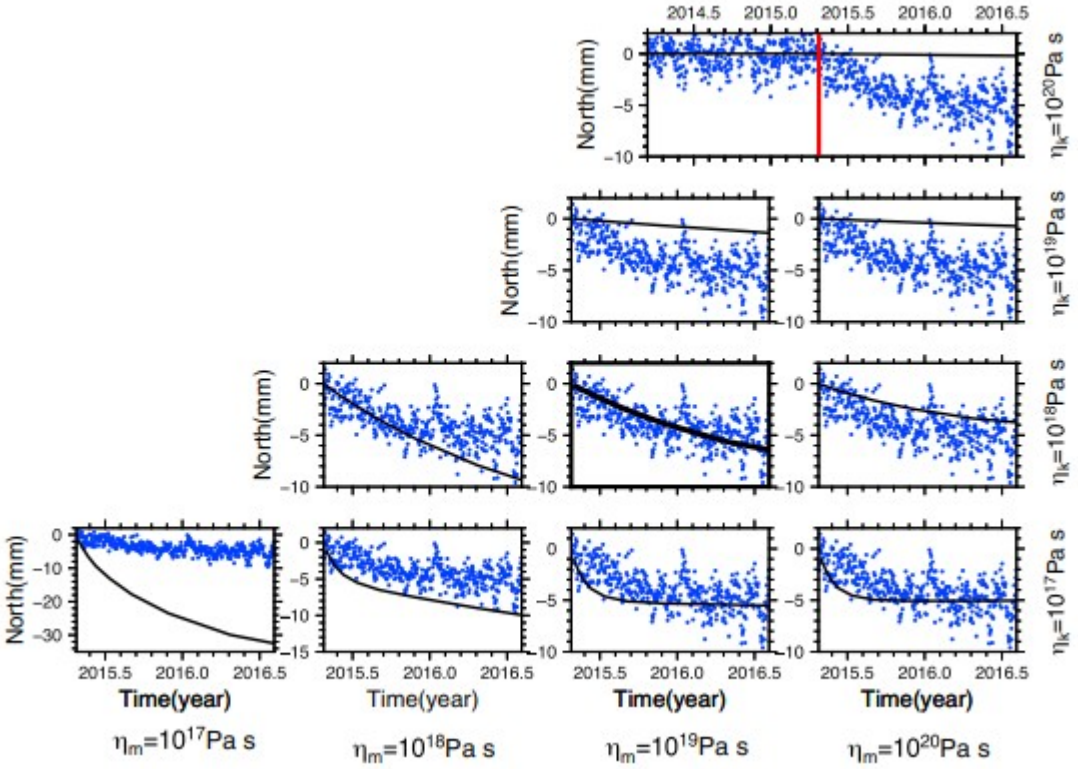

Figure 10

Position time series of postseismic transient southward motion in the first year at the far-field GPS station XZNM (blue dots) and the modeled curve (black lines) for various combinations of Tibetan mantle transient and steady state viscosities. The topmost panel shows the complete time series at this station, with the red vertical line representing the time of the mainshock. The bold box highlights the preferred model.

We perform a two-dimensional grid search to obtain optimal viscosities of the Tibet's upper mantle (Figure 10). The values of the transient viscosity (η_k^{UMT}) and steady state viscosity (η_m^{UMT}) beneath Tibet are varied from 10^{17} to 10^{20} Pa s in order-of-magnitude steps. Given that the transient viscosity of the Kelvin body is lower than or equal to that of the Maxwell component in the Burgers body, we only examine the cases when the η_m^{UMT} is greater or equal to η_k^{UMT} . The results show that predictions with a low transient viscosity of 10^{17} Pa s produce early motions that are too rapid, whereas displacements from models with η_k^{UMT} of 10^{19} Pa s underpredict the observations (Figure 10). The best fitting solution has a transient Kelvin viscosity of 1×10^{18} Pa s and a steady state Maxwell viscosity of 1×10^{19} Pa s (bold box in Figure 10). Because we assume that the postseismic deformation at XZNM is solely

driven by viscous flow in the upper mantle and exclude the potential contributions from the lower crustal flow and afterslip, this order-of-magnitude estimate provides a lower bound.

4.4.3 Lower Crustal Viscosity Beneath Southern Tibet

Compared to the more commonly used homogeneous layered rheological structure, more parameters affect the results when employing a heterogeneous rheological structure, such as the model geometry parameter (D in Figure 4) and the thickness of the elastic upper layer of southern Tibet (W_e). Here we show the results from our first-order approximation of the heterogeneous rheological structure, in which the viscosities in the upper mantle beneath India and Tibet are fixed to the values found in sections 4.4.1 and 4.4.2. Initially, the distance D from the MFT to Tibet's lithosphere is held at 167 km, based on the location of the transition to low electrical resistivity in southern Tibet along a margin-perpendicular magnetotelluric survey profile across the epicentral region (Unsworth et al., 2005). In the multiple-mechanism models we consider below, we will further examine the trade-off between D and η_m^{LCT}. For the sake of simplicity, we assume the ratio of the steady state transient viscosity η_m^{LCT} to the transient viscosity η_k^{LCT} in the Burgers body is a constant and follow Hu, Bürgmann, Banerjee, et al. (2016) and Hu, Bürgmann, Uchida, et al. (2016) and use $\eta_m^{\mathrm{LCT}}/\eta_k^{\mathrm{LCT}} = 10$, which is also the same value we obtain for the upper mantle beneath Tibet.

We fix the Moho depth in Tibet at 70 km and vary W_e from 20 to 50 km. We consider a variety of steady state viscosities ranging from 2×10^{18} to 1×10^{22} Pa s. We first attempt to constrain η_m^{LCT} using all available GPS observations in southern Tibet and in Nepal. In this case, the optimal solution favors a low $\eta_m^{\mathrm{LCT}} = 4 \times 10^{18}$ Pa s, corresponding to a large WRMS misfit of 13.0 mm, a clear indication that viscoelastic relaxation alone cannot be responsible for the observed deformation. The inferred surface displacements are incapable of matching the near- and far-field observations simultaneously, resulting in overestimated displacements in southern Tibet and underestimated deformation in northern Nepal. This poor constraint on η_m^{LCT} when using all GPS data motivates us to constrain η_m^{LCT} with the southern Tibet stations alone.

The η_m^{LCT} is determined by minimizing the data misfit calculated for each elastic thickness using the 1 year displacements of the six stations in southern Tibet (Figure 1). The best fit steady state viscosity decreases with increasing elastic thickness, ranging from a viscosity of 8×10^{19} Pa s for a 20 km thick elastic layer to a viscosity of 1×10^{19} Pa s for W_e = 50 km (Figure 11). The modeling results favor a thinner elastic layer thickness, but the WRMS misfit curve for W_e = 30 km (green line in Figure 11) is very close to that for W_e = 20 km. Even though the WRMS misfit of the model with W_e = 20 km is slightly smaller than that with W_e = 30 km, the multiple-mechanism models with W_e = 20 km perform worse than those with Tibet's elastic thickness at 30 km. In addition, the 30 km elastic thickness agrees with the upper bound inferences constrained from Holocene shoreline deflections around Siling Co (Figure 1), central Tibet, which is located in the northeast corner of our study region (Shi et al., 2015). Therefore, we assign the elastic thickness of Tibet to be 30 km, $\eta_m^{LCT} = 6 \times 10^{19}$ Pa s and $\eta_k^{LCT} = 6 \times 10^{18}$ Pa s. Although the optimal viscous model cannot explain the near-field observations in Nepal, its prediction exhibits good agreement with observations in the southern Tibetan Plateau with a very small misfit of 2.7 mm. The unmatched displacements in the near field are probably due to other mechanisms, in particular, afterslip.

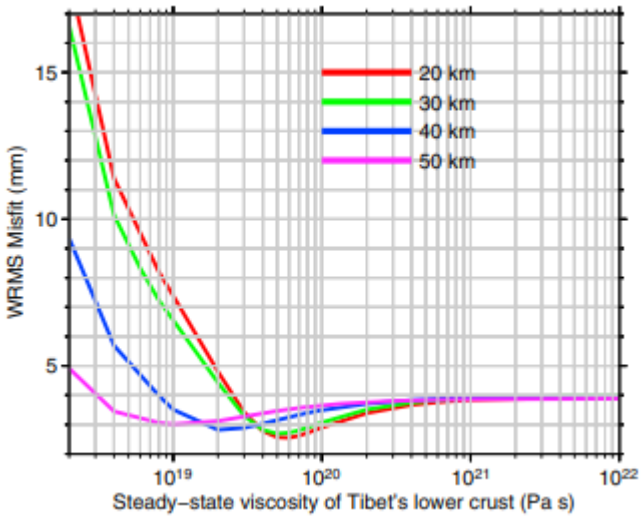

Figure 11

WRMS misfit to the GPS observations in southern Tibet of the viscoelastic model as a function of the steady state viscosity in the lower crust beneath the southern Tibetan Plateau (the transient viscosity is fixed at one tenth of the steady state value). This model includes contributions from upper mantle relaxation in Tibet and India at their preferred values. The Tibetan Moho depth is fixed at 70 km and

the distance from the MFT to the Tibetan lithosphere (D) is set to 167 km. Solid lines in different colors represent the results for different elastic layer thicknesses (W_e) in southern Tibet.

4.5 Multiple Mechanisms

Our modeling of the poroelastic rebound, afterslip (kinematic model and stress-driven model), and viscoelastic relaxation allows us to conclude that no single mechanism satisfactorily explains the observed postseismic deformation following the Gorkha earthquake. Although the kinematic afterslip model shows good agreement with observations especially in the horizontal component, the inversion favors a very broad distribution and afterslip that reaches far downdip of the rupture, which is found to be physically implausible based on calibrated stress-driven afterslip models. In addition, neither viscoelastic relaxation nor poroelastic rebound models can satisfactorily explain both the near- and far-field observations.

We attempt to determine multiple-mechanism models following a schematic flowchart as depicted in Figure 5. For the viscoelastic relaxation models, we set η_k^{UMT} to 1×10^{18} Pa s and η_m^{UMT} to 1×10^{19} Pa s, which are inferred from data at the far-field GPS station XZNM (see section 4.4.2), and keep the η_m^{UMT} to be 10^{20} Pa s (see section 4.4.1). We investigate a range of values for the viscosity of Tibet's lower crust, η_m^{LCT}, and the distance between the MFT and Tibet lithosphere, D, which govern the pattern and amplitude of the near-field relaxation signal. We consider η_m^{LCT} values ranging from 2×10^{18} to 10^{20} Pa s, and D is varied from 110 to 350 km. The transient viscosity η_m^{LCT} is set to one tenth of the given steady state value. Additionally, since the hydraulic diffusivity of the uppermost crust remains uncertain, we examine different poroelastic rebound displacements with hydraulic diffusivity values varying from 0.1 to 1.0 m^2/s.

We find that it always makes the misfit worse when contributions from poroelastic rebound models are incorporated in the multiple-mechanism models. Figure S11 shows an example of WRMS misfit and afterslip centroid distance parameter variations as a function of hydraulic diffusivity in the multilayered earth structure. As afterslip dominates the near-field deformation (Figure S9) where potential contributions from poroelastic rebound are largest (Figure 3), we keep the viscoelastic parameters at their preferred values (Figure 13), which are determined in the following section, in this analysis. Therefore, we only consider the afterslip and viscoelastic rebound models in the final multiple-mechanism models shown below.

Figure 12a illustrates the residual misfit distribution (WRMS for KAM + VEM (kinematic afterslip model + viscoelastic relaxation model) as a function of model geometry parameter D and steady state viscosity of Tibet's lower crust. The residual misfit generally increases with decreasing D and η_m^{LCT} values. A wide area (blue zone in Figure 12a) of the rheological parameter space {D, η_m^{LCT}} allows for low residual misfit, where WRMS values are no more than 4.8 mm, which is the misfit value of the pure afterslip model. In

other words, it is difficult to constrain D and η_m^{LCT} based solely on data misfit. This is due to the inherent trade-off of viscoelastic relaxation and afterslip and probably also the sparse distribution of available GPS stations in the southern Tibetan Plateau.

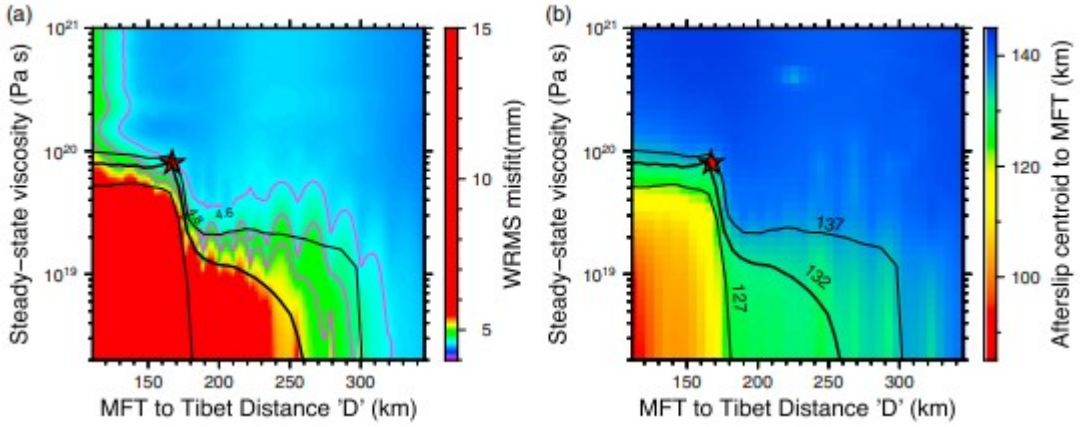

Figure 12

(a) WRMS misfit of multiple-mechanism models (KAM + VEM) considering the viscosity of the lower crust beneath southern Tibet and model geometry parameter *D* (Figure 4). Magenta lines follow 4.6, 4.8, and 5.0 mm contours of the WRMS misfit. (b) Distance between the residual afterslip centroid of multiple-mechanism models and the MFT. Red stars show the preferred values of *D* and the steady state viscosity of Tibet's lower crust. Black contour lines show 127–137 km interval of the slip centroid distance-from-MFT, and the middle bold line represents the preferred value of 132 km.

The stress-driven afterslip model can be used to assess which kinematic afterslip models are physically meaningful (Huang et al., 2014). As shown in Figure 7b, the stress-driven afterslip model favors a narrower and shallower slip distribution than the kinematic model inverted from the GPS data. The W_{MFT}^{SC} of the kinematic afterslip model is 153 km, and that of the stress-driven afterslip model is only 132 km. Figure 12b shows the color-contoured values of the residual afterslip centroid distance-from-MFT for the same suite of viscous models considered in Figure 12a. The W_{MFT}^{SC} varies from 85 to 145 km (Figure 12b). When W_{MFT}^{SC} is close to 85 km, it means that the residual afterslip distribution nearly overlaps with the coseismic rupture. On the contrary, when the W_{MFT}^{SC} grows to 145 km, it indicates the afterslip distribution is far from the rupture. Both of these end-member cases are physically implausible. The preferred stress-driven afterslip model (SDAM) yields a moderate W_{MFT}^{SC} of ~132 km (Figure 7b). The bold black contour line in Figure 12b shows the models for which W_{MFT}^{SC} = 132 km.

When considering both the WRMS misfit and the afterslip centroid distance-from-MFT together (Figure 12), satisfactory rheological model values {D, η_m^{LCT}}

are constrained within a relatively narrow range. In Figure 12, the bold black contour lines highlight the models with the preferred distance between afterslip centroid and the MFT of the stress-driven model of ~132 km, and the gray lines show the residual WRMS contours between 4.6 and 5.0 mm. The overlapping segment between the black line and white contours shows the narrowed ranges of preferred values of D and η_m^{LCT}. The representative model, whose W_{MFT}^{SC} is close to that of the stress-driven afterslip model (~132 km), has D = 167 km and $\eta_m^{LCT} = 8 \times 10^{19}$ Pa s (red stars in Figure 12 and illustrated in Figure 13). The η_m^{LCT} obtained here is slightly higher than the value of 6×10^{19} Pa s constrained in section 4.4.3. There is an important trade-off between the model geometry parameter D and the steady state viscosity of Tibet's lower crust η_m^{LCT}.

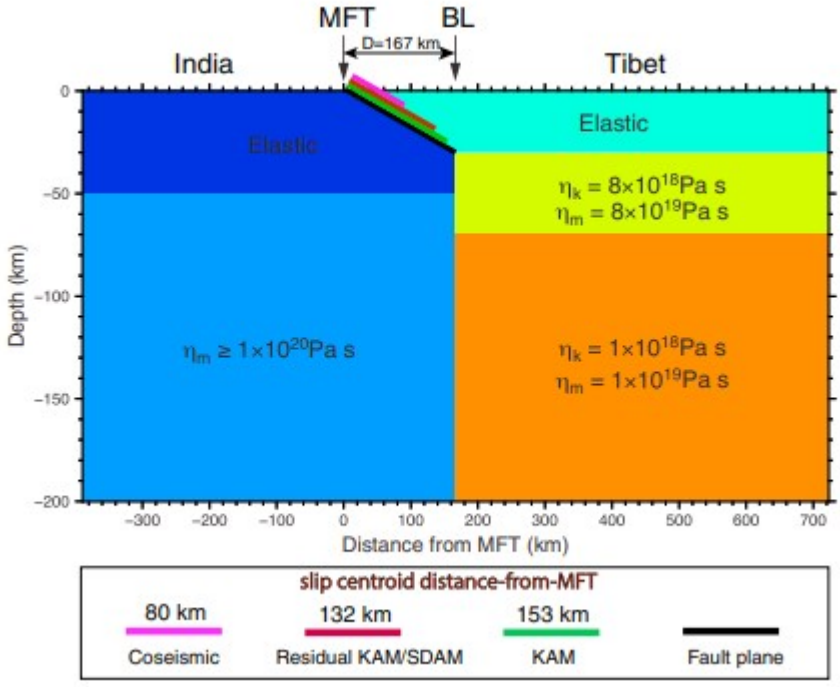

Figure 13

First-order approximation of the preferred laterally heterogeneous rheological structure based on the multiple-mechanism model. Slip-centroid distance from the MFT ( ) for coseismic, kinematic afterslip only (KAM), and the residual kinematic (KAM) and stress-driven afterslip (SDAM) models are illustrated on the fault plane coded in different color and length.

The final residual afterslip model obtained by inverting the residuals of the inferred viscoelastic model (Figure 13) is shown in Figure 14. The slip distribution becomes more compact than the initial kinematic afterslip model (KAM) inversion (Figure 7a), leaving no aseismic slip at the bottom of the

fault plane deep under South Tibet. The afterslip centroid distance-from-MFT decreases from 153 km in the initial afterslip model to ~132 km in the VEM + KAM multiple-mechanism model, as only very small displacements are left in southern Tibet after correcting for the viscoelastic effects. The residual afterslip model produces a moment release of 5.5×10^{19} Nm, equivalent to M_w7.16, about 45% less than the afterslip-only model. Though the misfit of the preferred multiple-mechanism model is slightly smaller than the kinematic afterslip model, it is more physically reasonable.

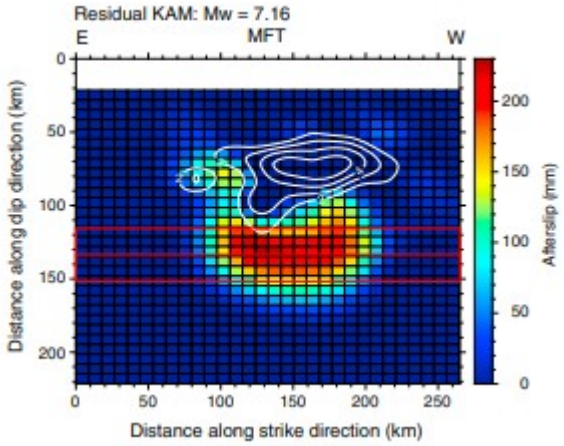

Figure 14

Residual kinematic afterslip distribution after correcting for viscoelastic relaxation by employing the inferred rheological structure in Figure 13. The 1 m slip contour lines of the mainshock and *M*7.3 aftershock are shown in white. Red boxes show the centroid distance (the middle lines) and ranges within which 50% of the moment lies in this model.

Figure 15 depicts the comparison between observed initial 1 year postseismic displacements and calculated viscoelastic relaxation and afterslip by using the preferred rheological structure (Figure 13) and afterslip model (Figure 14). The results show that the initial 1 year postseismic deformation following the Gorkha, Nepal, earthquake can be well explained by downdip afterslip and viscous relaxation in the lower crust and upper mantle.

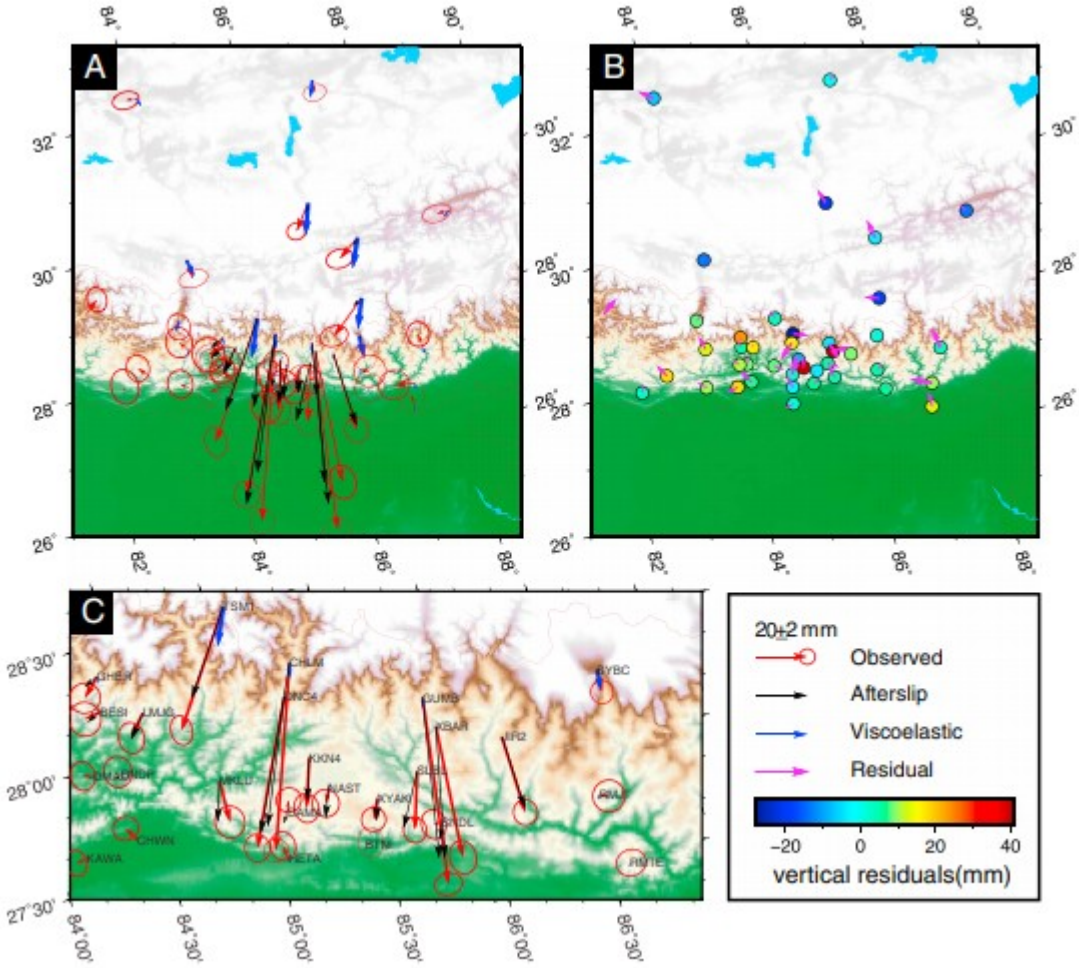

Figure 15

(a) Comparison of GPS observed (read arrows with 95% confidence ellipses) and calculated horizontal displacements due to viscoelastic relaxation (blue arrows) and afterslip (black arrows) model contributions. (b) Residuals between the observed and modeled 1 year displacements from both viscoelastic relaxation and afterslip. Colored circles show the vertical component of residuals and magenta arrows represent the horizontal residuals. As discussed in the text, our preferred multiple-mechanism model does not include contributions from poroelastic rebound. (c) Zoom of Figure 15a in the rupture area.

5 Discussion

5.1 Vertical Deformation Pattern

Vertical displacements have often been deemed as the key observations to discriminate viscous relaxation and afterslip models, especially for strike-slip mechanisms (e.g., Hearn, 2003). For instance, only upper mantle flow can explain the lobate pattern of observed InSAR line-of-sight range changes following the Mojave Desert earthquakes (Bürgmann & Dresen, 2008; Pollitz, 2003; Pollitz, et al., 2001), which are opposite to contributions from lower crustal afterslip models. Different postseismic mechanisms show different patterns of vertical displacements in the first 1 year after the Gorkha

earthquake (Figures S9 and S10). The afterslip models predict uplift in the north and subsidence in the south (Figure S9). The hinge line separating the opposite sign of vertical displacements moves to farther north when the afterslip centroid goes deeper. Contributions from viscoelastic rebound show a very wide area of uplift in Tibet Plateau with peak value of ~12 mm and small subsidence in Nepal (Figure S10b). The poroelastic rebound models (Figure S10d) exhibit a somewhat similar vertical deformation pattern covering a much smaller area, compared to the viscoelastic relaxation models.

The observed postseismic vertical GPS measurements are characterized by peak uplift in north Nepal (Figure 2). Due to the sparsity of GPS stations, the vertical deformation pattern is uncertain in South Tibet. Vertical contributions from viscoelastic rebound models are opposite to GPS observations. Poroelastic rebound models can produce significant uplift in northern Nepal but fail to fit observations in the southern Nepal. Our afterslip models (kinematic model and stress-driven model) and multiple-mechanism model can explain the first-order vertical displacement pattern. However, there are still large residuals at several stations that cannot be easily explained by additional contributions from viscous relaxation and poroelastic rebound (Figure 15b). The large misfit in the vertical deformation could be attributed to multiple possible sources. The first one is the stability of the survey marker. As we have pointed out, several stations located in the Kathmandu Basin are seriously affected by land subsidence due to groundwater depletion. A second problem is that the time span interval may be too short to reliably record the transient vertical deformation. There are at least five stations in Nepal with no more than 10 month's records. The third issue is our limited knowledge of the seasonal deformation at newly established stations and ignoring tectonic vertical deformation in this region. Although our models do not fully match the vertical component due to the above potential factors, it is clear that the most important mechanism producing vertical motions during the first year after the Gorkha earthquake is aseismic afterslip, only it can fit the first-order vertical deformation. Denser GPS station distribution, possibly aided by InSAR measurements, and longer GPS time series should improve future investigations of this issue.

5.2 Comparison With Previous Afterslip Models

Several afterslip models have been published to understand the earlier postseismic mechanisms based on GPS observations in Nepal and/or very short intervals of InSAR data (Gualandi et al., 2016; Mencin et al., 2016; Sreejith et al., 2016). These studies only consider afterslip alone as the postseismic mechanism and ignore contributions from other mechanisms including viscous relaxation and poroelastic rebound. Sreejith et al. (2016) inferred a downdip afterslip distribution based on kinematic inversion of only 12 days of InSAR data and 13 days of GPS observations at four Nepal stations starting 4 days after the mainshock, finding a gap between the coseismic and afterslip slip zones. Such a slip pattern with a large spatial

separation of the coseismic and afterslip is hard to understand using physically reasonable stress-driven afterslip models, which shows that slip should occur immediately beneath the main asperity (Figure 7b). Our preferred kinematic afterslip-only model without the rupture exclusion constraint (Figure S9a) produces a similar spatial distribution as that of Gualandi et al. (2016), featuring a very broad slip distribution and afterslip far downdip of the rupture. The downdip end of the inverted afterslip-only model is over 200 km away from the MFT, where the temperature exceeds 800°C according to the thermal structure model by Ader et al. (2012) based on data from Herman et al. (2010). Such high temperatures put this zone below the brittle-ductile transition of even mafic crustal rocks. Our stress-driven afterslip models also do not support the far downdip slip found in afterslip-only inversions.

If viscous contributions are ignored in kinematic afterslip inversions large values of afterslip are obtained at greater depths (e.g., Freed et al., 2006). After correcting for viscoelastic relaxation in the lower crust and upper mantle beneath Tibetan Plateau, we obtain a more physically reasonable and shallower afterslip distribution (Figure 14), which is consistent with the stress-driven afterslip model.

5.3 Implications of Low Moment Release of Afterslip

The afterslip-only model moment release equals 1.0×10^{20} Nm within the first year following the Gorkha earthquake. It decreases to 5.5×10^{19} Nm after correcting for the viscous relaxation from the observations. Therefore, only ~7% of the coseismic moment has been released after 1 year. Gualandi et al. (2016) find that about 17% coseismic moment is released within 7 months through aseismic afterslip, ignoring the contributions from viscoelastic relaxation. Their higher value of afterslip-to-coseismic fraction is also related to their choice of a wider fault geometry and to only using data from Nepal.

Afterslip has been observed immediately after large and moderate earthquakes in different seismotectonic settings and releases a very wide range of the fraction of the mainshock moment (e.g., Villegas-Lanza et al., 2016). Table 1 summaries the range of ratios between afterslip and coseismic moment following several well studied earthquakes. The shallow afterslip in the first few years following the 2004 *M*6 Parkfield, California, earthquake released more than 200% of the coseismic moment (Freed, 2007; Langbein et al., 2006). In some other moderate events, such high moment release ratios have also been documented (Fattahi et al., 2015). On the other hand, downdip afterslip in the first 14 months after the 1999 Chi-Chi earthquake only released 7% of the coseismic moment (Hsu et al., 2002). For the 2001 Kokoxili, 2003 Bam, and 2008 Wenchuan events, relatively low ratios are also estimated within the first few years (Huang et al., 2014; M. H. Huang, personal communication, 2017; Ryder et al., 2011; Tan et al., 2013; Wimpenny, et al., 2017).

Table 1
Fraction of the Coseismic Moment Released by Afterslip for a Selection of Earthquakes

Earthquake	Coseismic moment magnitude	Fraction of coseismic moment	Shallow afterslip(SA)/ downdip afterslip(DA)	Article
2004 Parkfield, California	6.0	>200% in 8 months and 300% in 2 years	SA	Langbein (2006) and Freed (2007)
2007 Ghazaband, Pakistan	5.5	70% in 1 year	SA	Fattahi et al. (2015)
2011 Tohoku-Oki, Japan	9.0	10% in 2 weeks, 21% in 2.5 years, and >30% in 2 years	SA, SA & DA, and SA	Ozawa (2011), Yamagiwa et al. (2015) and Hu, Bürgmann, Uchida et al. (2016)
2005 Nias, Indonesia	8.7	>25% in 11 months and 50% in 6 months	SA and DA	Hsu et al. (2006) and Kreemer et al. (2006)
1999 Izmit, Turkey	7.5	26% in 3 months	SA and DA	Bürgmann et al. (2002)
2008 Wenchuan, China	7.9	13% in 8 months and <8% in 1 year	SA and DA, and DA	Tan et al. (2013), Huang et al. (2014) and Huang (personal communication, 2017)
1999 Chi-Chi, Taiwan	7.6	7% in 14 months	DA	Hsu et al. (2002)
1997 Manyi, China	7.6	20% in 3 years	DA	Ryder et al. (2007)
2001 Kokoxili, China	7.9	8% in 1 year	DA	Ryder et al. (2011)
2015 Gorkha, Nepal	7.9	~7% in 1 year and 17% in 7 months	DA and DA	This study and Gualandi et al. (2016)

Afterslip represents the response of the unruptured fault to the stress changes induced by the coseismic rupture. The spatial distribution and temporal evolution of afterslip are strongly governed by the velocity-strengthening properties of the zone hosting the aseismic slip (e.g., Marone et al., 1991; Scholz, 1998). The frictional properties and velocity-strengthening behavior depend on a number of factors including the effective normal stress, the type of rock material, and temperature (e.g., Kaneko, et al., 2010). Table 1 shows that the afterslip-to-coseismic moment ratio is high when the afterslip predominately occurs at shallow depths on fault sections that were already known to be slipping aseismically during the interseismic period. However, the moment release ratio is low when the aseismic slips occur only in downdip portions. The afterslip following the Gorkha earthquake occurs primarily on the downdip section of the MHT, where temperatures exceed ~350°C (Ader et al., 2012) and conditions in the MHT fault zone may be quite ductile. The frictional properties of faults at high temperatures in the lower crust (Blanpied, et al., 1991) are quite different from shallow creeping faults. The lack of significant shallow afterslip suggests that the MHT at seismogenic depths has velocity-weakening frictional properties, is strongly coupled during the interseismic period (e.g., Ader et al., 2012), and accommodates most all of its slip budget in seismic ruptures. Time-dependent kinematic afterslip inversions show that shallow afterslip rapidly decays, whereas deep afterslip is more enduring (e.g., Bürgmann et al., 2002; Savage, et al., 2007). Hence, the low moment release ratio of afterslip triggered by the Gorkha earthquake, and the small percentage (17%) of the coseismic stress increase that has, so far, been released by deep afterslip (Figure 9), suggests long decay times and enduring afterslip following this event.

5.4 Implication for Earthquake Cycle Deformation in Central Nepal

During the interseismic period, the MHT in the central Nepal region appears fully locked from the surface to a depth of 17–24 km (locking width of 98–134 km from MFT, Table S1) based on geodetic observations (e.g., Bettinelli et

al., 2006; Bilham, et al., 1997; Feldl & Bilham, 2006; Grandin et al., 2012; Jouanne et al., 2004; Larson et al., 1999). The crust near the downdip edge of the locked MHT is the place that hosts most seismicity and above which the Higher Himalayan mountains uplift at a peak rate of about 6 mm/a in the interseismic period. More detailed inversions for distributed interseismic coupling find that the coupling pattern is quite homogeneous along the Nepal Himalaya (Ader et al., 2012; Stevens & Avouac, 2015). Interseismic coupling on the MHT is inferred to vary primarily in the downdip direction. The MHT appears nearly fully locked to the south of the front of the Higher Himalaya and fully creeping to the north of it. The transition from unstable to stable slip behavior can be related to the temperature at that depth (Ader et al., 2012). In contrast, in many subduction zones interseismic coupling is highly variable, indicative of heterogeneous fault friction properties (e.g., Avouac, 2015; Kaneko et al., 2013). This includes sections of very low coupling throughout the seismogenic depth range and near the trench.

The mainshock of the Gorkha earthquake ruptured the deeper portion of the fully locked segment of the MHT (coupling ratio larger than ~0.8) (Avouac et al., 2015; Elliott et al., 2016; Qiu et al., 2016; Wang & Fialko, 2015) and possibly also a shallow out-of-sequence thrust fault at the foot of the High Himalaya (Whipple et al., 2016). The downdip edge of the coseismic rupture reaches the bottom of the fully locked MHT, and the updip edge of the rupture ends at approximately 10 km beneath the surface (~60 km form the MFT). The partial rupture of the fully locked MHT can be attributed to the fault morphology (Qiu et al., 2016). Two weeks later the largest aftershock M_w7.3 aftershock occurred near the eastern edge of the mainshock. There is a small unruptured gap between these two rupture zones.

The Gorkha earthquake increases stresses away from the coseismic peak rupture zone, which are relieved through aseismic slip and consequently produce geodetically measureable postseismic displacements. Our multiple-mechanism models suggest that the deep downdip afterslip dominates during the first year. Results from the stress-driven and residual kinematic afterslip models (after correcting for contributions from the viscoelastic response) indicate slip occurs in the brittle-ductile transition zone, where the interseismic coupling ratio decreases from ~0.8 to ~0.2 and the temperature increases from 300 to 500°C (Ader et al., 2012). Similar downdip afterslips have been well documented following several continental thrust earthquakes (Hsu et al., 2002; Jouanne et al., 2011). In these examples, afterslip occurred mostly downdip of the seismic rupture, mainly within the transition zone between the fully locked and fully creeping zone rather than within the locked fault zone or updip zone. The locking width from the MFT (W_L = 95 km) inferred from the stress-driven afterslip model is shorter than the average fully coupled width from the MFT based on interseismic coupling models (Figure 9), suggesting that there is a component of afterslip near the base of the fully locked zone where coseismic slip was small. To first order,

the coseismic and postseismic slips occur on complementary parts of the MHT.

Within the theoretical framework of rate-and-state friction law, the frictional parameter ($a - b$) at shallow depths is positive because of the presence of unconsolidated granular material (Scholz, 1998). This is supported by evidence of almost no seismicity within shallow depths along many faults. This is not suitable for faults that are fully locked to the surface as suggested by Kaneko et al. (2013). Our afterslip models and previous published results (e.g., Gualandi et al., 2016) indicate that the unruptured shallow portion of the MFT appears still locked in the postseismic period. Considering that the shallower portion of the fault is fully locked both in the interseismic and postseismic period (e.g., Ader et al., 2012; Stevens & Avouac, 2015), we infer that the frictional parameter $a - b$ for the shallow portion of MFT is less than zero. This implies that the shallow portion has the capability to rupture alone or may be incorporated in a much larger earthquake involving neighboring segments of the MHT (Bilham et al., 2017). An evaluation of the detailed stress changes and seismic hazard in the shallow portion is beyond the scope of this paper; we will report on this topic in future contributions.

Our kinematic inversions, including both the afterslip-only model and residual afterslip model, also find slip in the unruptured small gap between the mainshock and the largest aftershock slip zones. A similar pattern of afterslip is also found and documented by Gualandi et al. (2016). A simple resolution test indicates that the slip on the small gap can be recovered (Figures S4g and S4h). This probably suggests that the small gap exhibits different frictional properties from its surrounding, which may be related to lateral variations of the coupling ratio in this zone (Stevens & Avouac, 2015).

Additionally, stress changes from the Gorkha earthquake also induced viscoelastic flow in the lower crust and upper mantle, which in turn produce crustal strain and geodetically measureable surface deformation. Our model invoking a first-order lateral rheological structure constrained by GPS observations predicts deformation transients across a wide region of southern Tibet and little deformation in northern India and in southern Nepal. According to the inferred steady state viscosities beneath Tibet, the viscoelastic transients will last for many decades.

5.5 Lateral Heterogeneous Rheological Structure

By analyzing postseismic deformation of the Gorkha earthquake, we constrain a simplified laterally heterogeneous rheological structure across India and Tibet (Figure 13). The effective viscosity of the upper mantle beneath India is poorly constrained, because no transient deformation was observed in North India following the Gorkha event. We put a lower bound of 10^{20} Pa s on the viscosity of the Indian mantle below 50 km constrained by the very low rate of northward displacements in southern Nepal. The effective elastic thickness of the lithosphere, T_e, is a proxy for the strength of continental lithosphere (Jackson, 2002). The Indian Plate in North India has

an average T_e value of 55 km (Audet & Bürgmann, 2011; Burov & Watts, 2006; Maggi et al., 2000), suggesting a strong high-viscosity mantle more similar to that found in cratonic plate interiors than in plate boundary zones (Bürgmann & Dresen, 2008). A high viscosity of the Indian upper mantle is also supported by other geophysical observations, including low resistivity inferred from magnetotelluric data (Unsworth et al., 2005), high seismic wave speeds (Li et al., 2008; Zhou & Murphy, 2005), and a low geothermal gradient of the Indian subcontinent (Herman et al., 2010).

Compared to the substantial thickness of the upper elastic layer and high upper mantle viscosity in India, the Tibetan lithosphere is weak with a viscously relaxing lower crust and upper mantle. This suggests a substantial rheological contrast between India and Tibet. A relatively weak Tibet lithosphere inferred from postseismic relaxation processes is also in good agreement with different kinds of evidence, such as low seismic wave speeds, high resistivity, and high temperature below South Tibet (Beaumont et al., 2001; Herman et al., 2010; Unsworth et al., 2005; Zhou & Murphy, 2005). The inferred transient and steady state viscosities of the lower crust and upper mantle beneath South Tibetan Plateau fall in the range of previously proposed effective viscosities 10^{17}–10^{20} Pa s, which are constrained by modeling postseismic deformation of events that occurred in the interior and along the eastern and northern margins of the Tibetan Plateau (e.g., Bendick et al., 2015; Huang et al., 2014; Ryder et al., 2010, 2011; Wang & Fialko, 2014; Wen et al., 2012). Our inferred effective viscosities in southern Tibet are more than 2 orders of magnitude greater than the extremely low viscosities of ~10^{16} Pa s that had been suggested to explain the uplift along the east edge of the Tibetan Plateau and have been invoked in support for the lower crustal channel flow hypothesis (Royden et al., 1997).

Studies on postseismic deformation following the Nima and Kokoxili earthquakes show that a weak lower crust and relatively stronger mantle are indicated to explain the InSAR and GPS data in the northern Tibetan Plateau (Ryder et al., 2011, 2010). At the eastern edge of the Tibetan Plateau, Huang et al. (2014) also proposed a similar rheological structure. However, our preferred rheological structure favors an upper mantle with a somewhat lower viscosity than the lower crust. One possible explanation for the difference is that the rheological structure indeed differs from that in northern Tibetan Plateau, related to low-angle subduction of the Indian Plate under the Eurasian Plate. Another possible reason is that the viscosities constrained in this study heavily rely on very sparse intermediate- and far-field GPS data in southern Tibet. More specifically, we use only one station to constrain the viscosities of Tibet's upper mantle. Considering that the near-field transients are still dominated by downdip afterslip, more refined estimates of viscosity should be possible based on longer and denser data in the coming years.

The thickness of the upper elastic layer of the Tibetan Plateau remains controversial, with estimates ranging from 15 to 30 km. The maximum depth of seismicity is limited to depths of ~15 km in interior Tibet, indicating a relatively thin elastic upper crust (Craig, et al., 2012; Liang et al., 2008; Molnar & Chen, 1983). Some postseismic deformation studies also favor an elastic thickness of no more than 20 km in the northern Tibetan Plateau (e.g., Ryder et al., 2011; Wen et al., 2012). However, the “long-term” estimate of T_e in Siling Co (Figure 1), central Tibet is constrained to be 20–30 km from millennial lake loading deformation (Shi et al., 2015). Such thicker results are comparable to values of 20–40 km deduced from gravity anomalies and topography (e.g., Chen et al., 2015). We test a suite of multiple-mechanism models with a thinner elastic layer of 20 km and find that they do not perform better than those using an elastic thickness of 30 km (Figure S12). The postseismic deformation seems to favor a thicker elastic layer in South Tibet. Effective viscosities in the crust gradually decrease with increasing temperature below the seismogenic zone (e.g., Yamasaki & Houseman, 2012) and rocks with viscosities $>\sim10^{20}$ Pa s would not substantially relax at the time scale of early postseismic relaxation. Yamasaki and Houseman (2012) estimate Maxwell time constants to be between 200 and 2,000 years at 20 km depth, indicating effectively elastic behavior at the time scale of our observations, consistent with our model results.

A number of evidences from resistivity, seismic wave speeds, and temperature profiles across the Himalaya support the strong difference of lithospheric properties between India and Tibet. However, it is still challenging to determine the subsurface plate boundary structure between the Indian and southern Tibetan lithospheres and the southern extent of the weak Tibetan lower crust (Herman et al., 2010; Li et al., 2008; Unsworth et al., 2005; Zhou & Murphy, 2005). Our inferred rheology structure sheds some light on this issue. The boundary inferred from this study locates 120–180 km north from the MFT. The boundary location shows a clear trade-off with the viscosity in the lower crust of Tibet. While the inferred boundary zone agrees with previous results, we acknowledge that the simple vertical boundary shown in Figure 13 is too simplified.

6 Conclusions

The three-dimensional deformation caused by the 2015 Gorkha, Nepal, earthquake is analyzed using 1 year GPS measurements both in Nepal and in southern Tibet. We have developed individual poroelastic rebound, afterslip, and viscous response models to understand the mechanisms that govern the observed transient deformation. We find that no single mechanism can explain the postseismic observations. Instead, a combination of contributing mechanisms of afterslip and viscoelastic relaxation is required. In our inferred multimechanism model, the inverted residual afterslip favors slip within the brittle-ductile zone immediately downdip of the coseismic rupture and fills the small gap between the mainshock and the largest aftershock slip

zone. The unruptured shallow zone of the fault remains locked in the postseismic period, and its frictional properties appear to be velocity weakening and allow for the possibility of additional seismic rupture. In contrast to results by Gualandi et al. (2016), the fraction of coseismic moment released by afterslip after correcting for the viscoelastic relaxation becomes only ~7% in the first year. This low moment release ratio seems to be related to the lack of afterslip across the seismogenic depth range, with deeper (downdip) afterslip in the brittle-ductile transition regime releasing a relatively small amount of slip.

Our multimechanism model also illuminates the laterally heterogeneous rheological structure between India and southern Tibetan Plateau. The upper mantle below the thick elastic Indian lithosphere appears to have a high effective viscosity of $\geq 10^{20}$ Pa s, whereas the steady state viscosities for the lower crust and upper mantle of Tibet are approximately 1 order of magnitude lower than that of northern India. Our model viscosities for Tibet are consistent with various estimates obtained in the interior and along the edges of the Tibetan Plateau. Predictions based on the inferred rheological structure reveal that geodetically measureable viscous relaxation occurs across a very wide region of southern Tibet and will last for many decades.

Acknowledgments

The data from the Nepal GPS network, which was deployed under a collaboration between the California Institute of Technology and the Department of Mines and Geology of Nepal, are provided by Jean-Philippe Avouac through UNAVCO (ftp://data-out.unavco.org). We also thank Roger Bilham, Rebecca Bendick, and David Mencin for providing data from four additional GPS sites in Nepal, which are also available from UNAVCO. GPS data in South Tibet are from CMONOC. We thank Jean-Philippe Avouac and two anonymous reviewers for thoughtful comments that improved the manuscript. GPS data are processed using GAMIT/GLOBK package. Finally, we thank Fred Pollitz for providing the newly developed code VISCO2.5D and for helpful instructions on running the program. All of the figures were generated using GMT software.

References

Ader, T., Avouac, J.-P., Liu-Zeng, J., Lyon-Caen, H., Bollinger, L., Galetzka, J., … Flouzat, M. (2012). Convergence rate across the Nepal Himalaya and interseismic coupling on the Main Himalayan Thrust: Implications for seismic hazard. *Journal of Geophysical Research*, 117, B04403. https://doi.org/10.1029/2011JB009071

Altamimi, Z., Collilieux, X., & Métivier, L. (2011). ITRF2008: An improved solution of the international terrestrial reference frame. *Journal of Geodesy*, 85(8), 457– 473.

Audet, P., & Bürgmann, R. (2011). Dominant role of tectonic inheritance in supercontinent cycles. *Nature Geoscience*, 4(3), 184– 187. https://doi.org/10.1038/ngeo1080

Avouac, J.-P. (2015). From geodetic imaging of seismic and aseismic fault slip to dynamic modeling of the seismic cycle. *Annual Review of Earth and Planetary Sciences*, 43(1), 233– 271. https://doi.org/10.1146/annurev-earth-060614-105302

Avouac, J.-P., Meng, L., Wei, S., Wang, T., & Ampuero, J.-P. (2015). Lower edge of locked main Himalayan thrust unzipped by the 2015 Gorkha earthquake. *Nature Geoscience*, 8(9), 708– 711.

Barbot, S., Fialko, Y., & Bock, Y. (2009). Postseismic deformation due to the M_w6.0 2004 Parkfield earthquake: Stress-driven creep on a fault with spatially variable rate-and-state friction parameters. *Journal of Geophysical Research*, 114, B07405. https://doi.org/10.1029/2008JB005748

Beaumont, C., Jamieson, R. A., Nguyen, M., & Lee, B. (2001). Himalayan tectonics explained by extrusion of a low-viscosity crustal channel coupled to focused surface denudation. *Nature*, 414(6,865), 738– 742.

Bendick, R., Khan, S. F., Bürgmann, R., Jouanne, F., Banerjee, P., Khan, M. A., & Bilham, R. (2015). Postseismic relaxation in Kashmir and lateral variations in crustal architecture and materials. *Geophysical Research Letters*, 42, 4375– 4383. https://doi.org/10.1002/2015GL064670

Bettinelli, P., Avouac, J.-P., Flouzat, M., Jouanne, F., Bollinger, L., Willis, P., & Chitrakar, G. R. (2006). Plate motion of India and interseismic strain in the Nepal Himalaya from GPS and DORIS measurements. *Journal of Geodesy*, 80(8), 567– 589.

Bettinelli, P., Avouac, J.-P., Flouzat, M., Bollinger, L., Ramillien, G., Rajaure, S., & Sapkota, S. (2008). Seasonal variations of seismicity and geodetic strain in the Himalaya induced by surface hydrology. *Earth and Planetary Science Letters*, 266, 332– 344.

Bie, L., Ryder, I., Nippress, S. E., & Bürgmann, R. (2014). Coseismic and post-seismicactivity associated with the 2008 M_w6.3 Damxung earthquake, Tibet, constrained by InSAR. *Geophysical Journal International*, 196(2), 788– 803.

Bilham, R., Larson, K., & Freymueller, J. (1997). GPS measurements of present-day convergence across the Nepal Himalaya. *Nature*, 386(6,620), 61– 64.

Bilham, R., Mencin, D., Bendick, R., & Bürgmann, R. (2017). Implications for elastic energy storage in the Himalaya from the Gorkha 2015 earthquake and other incomplete ruptures of the Main Himalayan Thrust. *Quaternary International*. https://doi.org/10.1016/j.quaint.2016.09.055

Blanpied, M. L., Lockner, D. A., & Byerlee, J. D. (1991). Fault stability inferred from granite sliding experiments at hydrothermal conditions. *Geophysical Research Letters*, 18(4), 609– 612.

Bürgmann, R., & Dresen, G. (2008). Rheology of the lower crust and upper mantle: Evidence from rock mechanics, geodesy, and field observations. *Annual Review of Earth and Planetary Sciences*, 36(1), 531– 567. https://doi.org/10.1146/annurev.earth.36.031207.124326

Bürgmann, R., Ergintav, S., Segall, P., Hearn, E. H., Mcclusky, S., Reilinger, R. E., … Zschau, J. (2002). Time-dependent distributed afterslip on and deep below the Izmit earthquake rupture. *Bulletin of the Seismological Society of America*, 92(1), 126– 137.

Burov, E., & Watts, A. (2006). The long-term strength of continental lithosphere: “jelly sandwich” or “crème brûlée”? *GSA Today*, 16(1), 4.

Chanard, K., Avouac, J.-P., Ramillien, G., & Genrich, J. (2014). Modeling deformation induced by seasonal variations of continental water in the Himalaya region: Sensitivity to Earth elastic structure. *Journal of Geophysical Research: Solid Earth*, 119, 5097– 5113. https://doi.org/10.1002/2013JB010451

Chen, B., Liu, J., Chen, C., Du, J., & Sun, Y. (2015). Elastic thickness of the Himalayan–Tibetan orogen estimated from the fan wavelet coherence method, and its implications for lithospheric structure. *Earth and Planetary Science Letters*, 409, 1– 14.

Craig, T. J., Copley, A., & Jackson, J. (2012). Thermal and tectonic consequences of India underthrusting Tibet. *Earth and Planetary Science Letters*, 353–354, 231– 239.

Elliott, J., Jolivet, R., González, P., Avouac, J.-P., Hollingsworth, J., Searle, M., & Stevens, V. (2016). Himalayan megathrust geometry and relation to topography revealed by the Gorkha earthquake. *Nature Geoscience*, 9(2), 174– 180.

Fattahi, H., Amelung, F., Chaussard, E., & Wdowinski, S. (2015). Coseismic and post-seismic deformation due to the 2007 *M*5.5 Ghazaband fault earthquake, Balochistan, Pakistan. *Geophysical Research Letters*, 42, 3305–3312. https://doi.org/10.1002/2015GL063686

Feldl, N., & Bilham, R. (2006). Great Himalayan earthquakes and the Tibetan Plateau. *Nature*, 444(7,116), 165– 170.

Fialko, Y. (2004). Evidence of fluid-filled upper crust from observations of postseismic deformation due to the 1992 M_w7.3 Landers earthquake. *Journal of Geophysical Research*, 109, B08401. https://doi.org/10.1029/2004JB002985

Freed, A. M. (2007). Afterslip (and only afterslip) following the 2004 Parkfield, California, earthquake. *Geophysical Research Letters*, 34, L06312. https://doi.org/10.1029/2006GL029155

Freed, A. M., Bürgmann, R., Calais, E., & Freymueller, J. (2006). Stress-dependent power-law flow in the upper mantle following the 2002 Denali, Alaska, earthquake. *Earth and Planetary Science Letters*, 252(3–4), 481–489. https://doi.org/10.1016/j.epsl.2006.10.011

Freed, A. M., Herring, T., & Bürgmann, R. (2010). Steady-state laboratory flow laws alone fail to explain postseismic observations. *Earth and Planetary Science Letters*, 300, 1– 10. https://doi.org/10.1016/j.epsl.2010.10.005

Fu, Y., & Freymueller, J. T. (2012). Seasonal and long-term vertical deformation in the Nepal Himalaya constrained by GPS and GRACE measurements. *Journal of Geophysical Research*, 117, B03407. https://doi.org/10.1029/2011JB008925

Galetzka, J., Melgar, D., Genrich, J. F., Geng, J., Owen, S., Lindsey, E. O., … Maharjan, N. (2015). Slip pulse and resonance of Kathmandu basin during the 2015 M_w7.8 Gorkha earthquake, Nepal imaged with geodesy. *Science*, 349(6,252), 1091– 1095.

Grandin, R., Doin, M.-P., Bollinger, L., Pinel-Puyssegur, B., Ducret, G., Jolivet, R., & Sapkota, S. N. (2012). Long-term growth of the Himalaya inferred from interseismic InSAR measurement. *Geology*, 40(12), 1059– 1062. https://doi.org/10.1130/G33154.1

Gualandi, A., Avouac, J.-P., Galetzka, J., Genrich, J. F., Blewitt, G., Adhikari, L. B., … Liu-Zeng, J. (2016). Pre-and post-seismic deformation related to the 2015, M_w7. 8 Gorkha earthquake, Nepal. *Tectonophysics*. https://doi.org/10.1016/j.tecto.2016.06.0140040-1951

Gunawan, E., Sagiya, T., Ito, T., Kimata, F., Tabei, T., Ohta, Y., … Sugiyanto, D. (2014). A comprehensive model of postseismic deformation of the 2004 Sumatra-Andaman earthquake deduced from GPS observations in northern Sumatra. *Journal of Asian Earth Sciences*, 88, 218– 229.

Hearn, E. H. (2003). What can GPS data tell us about the dynamics of post-seismic deformation? *Geophysical Journal International*, 155(3), 753– 777. https://doi.org/10.1111/j.1365-246X.2003.02030.x

Hearn, E. H., Bürgmann, R., & Reilinger, R. E. (2002). Dynamics of Izmit earthquake postseismic deformation and loading of the Düzce earthquake hypocenter. *Bulletin of the Seismological Society of America*, 92(1), 172–193.

Herman, F., Copeland, P., Avouac, J.-P., Bollinger, L., Mahéo, G., Le Fort, P., … Henry, P. (2010). Exhumation, crustal deformation, and thermal structure of the Nepal Himalaya derived from the inversion of thermochronological and thermobarometric data and modeling of the topography. *Journal of*

Geophysical Research: Solid Earth, 115, B06407. https://doi.org/10.1029/2008JB006126

Herring, T. A., King, R. W., Floyd, M. A., & McClusky, S. C. (2015). Introduction to GAMIT/GLOBK, Release 10.6, Massachusetts Institute of Technology, Cambridge.

Hetényi, G., Cattin, R., Brunet, F., Bollinger, L., Vergne, J., Nábělek, J. L., & Diament, M. (2007). Density distribution of the India Plate beneath the Tibetan Plateau: Geophysical and petrological constraints on the kinetics of lower-crustal eclogitization. *Earth and Planetary Science Letters*, 264(1–2), 226– 244.

Hsu, Y., Bechor, N., Segall, P., Yu, S., Kuo, L., & Ma, K. (2002). Rapid afterslip following the 1999 Chi-Chi, Taiwan earthquake. *Geophysical Research Letters*, 29(16), 1754. https://doi.org/10.1029/2002GL014967

Hsu, Y. J., Simons, M., Avouac, J.-P., Galetzka, J., Sieh, K., Chlieh, M., … Bock, Y. (2006). Frictional afterslip following the 2005 Nias-Simeulue earthquake, Sumatra. *Science*, 312(5,782), 1921– 1926.

Hu, Y., Bürgmann, R., Banerjee, P., Feng, L., Hill, E. M., Ito, T., … Wang, K. (2016). Asthenosphere rheology inferred from observations of the 2012 Indian Ocean earthquake. *Nature*, 538, 368– 372. https://doi.org/10.1038/nature19787

Hu, Y., Bürgmann, R., Uchida, N., Banerjee, P., & Freymueller, J. T. (2016). Stress-driven relaxation of heterogeneous upper mantle and time-dependent afterslip following the 2011 Tohoku earthquake. *Journal of Geophysical Research: Solid Earth*, 121, 385– 411. https://doi.org/10.1002/2015JB012508

Huang, M.-H., Bürgmann, R., & Freed, A. M. (2014). Probing the lithospheric rheology across the eastern margin of the Tibetan Plateau. *Earth and Planetary Science Letters*, 396, 88– 96.

Huang, M.-H., Bürgmann, R., & Pollitz, F. (2016). Lithospheric rheology constrained from twenty-five years of postseismic deformation following the 1989 M_w6.9 Loma Prieta earthquake. *Earth and Planetary Science Letters*, 435, 147– 158.

Ingebritsen, S., & Manning, C. E. (1999). Geological implications of a permeability-depth curve for the continental crust. *Geology*, 27(12), 1107– 1110.

Jackson, J. (2002). Strength of the continental lithosphere: time to abandon the jelly sandwich?, *GSA Today*, 12(9), 4– 9.

Johnson, K. M., Bürgmann, R., & Larson, K. (2006). Frictional properties on the San Andreas fault near Parkfield, California, inferred from models of afterslip following the 2004 earthquake. *Bulletin of the Seismological Society of America*, 96(4B), S321– S338.

Jonssón, S., Segall, P., Pedersen, R., & Björnsson, G. (2003). Post-earthquake ground movements correlated to pore-pressure transients. *Nature*, 424(6,945), 179– 183.

Jouanne, F., Mugnier, J. L., Gamond, J. F., Le Fort, P., Pandey, M. R., Bollinger, L., … Avouac, J. P. (2004). Current shortening across the Himalayas of Nepal. *Geophysical Journal International*, 157, 1– 14.

Jouanne, F., Awan, A., Madji, A., Pêcher, A., Latif, M., Kausar, A., … Khan, N. A. (2011). Postseismic deformation in Pakistan after the 8 October 2005 earthquake: Evidence of afterslip along a flat north of the Balakot-Bagh thrust. *Journal of Geophysical Research*, 116, B07401. https://doi.org/10.1029/2010JB007903

Kaneko, Y., Avouac, J.-P., & Lapusta, N. (2010). Towards inferring earthquake patterns from geodetic observations of interseismic coupling. *Nature Geoscience*, 3(5), 363– 369.

Kaneko, Y., Fialko, Y., Sandwell, D. T., Tong, X., & Furuya, M. (2013). Interseismic deformation and creep along the central section of the North Anatolian fault (Turkey): InSAR observations and implications for rate-and-state friction properties. *Journal of Geophysical Research: Solid Earth*, 118, 316– 331. https://doi.org/10.1029/2012JB009661

Kreemer, C., Blewitt, G., & Maerten, F. (2006). Co- and postseismic deformation of the 28 March 2005 Nias M_w8.7 earthquake from continuous GPS data. *Geophysical Research Letters*, 33, L07307. https://doi.org/10.1029/2005GL025566

Langbein, J., Murray, J. R., & Snyder, H. A. (2006). Coseismic and initial postseismic deformation from the 2004 Parkfield, California, earthquake, observed by Global Positioning System, electronic distance meter, creepmeters, and borehole strainmeters. *Bulletin of the Seismological Society of America*, 96(4B), S304– S320. https://doi.org/10.1785/0120050823

Larson, K. M., Bürgmann, R., Bilham, R., & Freymueller, J. T. (1999). Kinematics of the India-Eurasia collision zone from GPS measurements. *Journal of Geophysical Research*, 104(B1), 1077– 1093.

Li, C., Van der Hilst, R. D., Meltzer, A. S., & Engdahl, E. R. (2008). Subduction of the Indian lithosphere beneath the Tibetan Plateau and Burma. *Earth and Planetary Science Letters*, 274(1), 157– 168.

Li, Q., You, X. Z., Yang, S. M., Du, R. L., Qiao, X. J., Zou, R., & Wang, Q. (2012). A precise velocity field of tectonic deformation in China as inferred from intensive GPS observations (in Chinese). *Science China Earth Sciences*, 55, 695– 698.

Liang, X., Zhou, S., Chen, Y., Lin, G., Xiao, L., Liu, P., … Ning, J. (2008). Earthquake distribution in southern Tibet and its tectonic implications.

Journal of Geophysical Research, 113, B12409. https://doi.org/10.1029/2007JB005101

Lindsey, E. O., Natsuaki, R., Xu, X., Shimada, M., Hashimoto, M., Melgar, D., & Sandwell, D. T. (2015). Line-of-sight displacement from ALOS-2 interferometry: M_w7.8 Gorkha earthquake and M_w7.3 aftershock. *Geophysical Research Letters*, 42(16), 6655– 6661.

Maggi, A., Jackson, J., Mckenzie, D., & Priestley, K. (2000). Earthquake focal depths, effective elastic thickness, and the strength of the continental lithosphere. *Geology*, 28(6), 495– 498.

Marone, C. J., Scholz, C. H., & Bilham, R. (1991). On the mechanics of earthquake afterslip. *Journal of Geophysical Research*, 96(B5), 8441– 8452.

Mazzotti, S., Dragert, H., Hyndman, R. D., Miller, M. M., & Henton, J. A. (2002). GPS deformation in a region of high crustal seismicity: N. Cascadia forearc. *Earth and Planetary Science Letters*, 198, 41– 48.

Mencin, D., Bendick, R., Upreti, B. N., Adhikari, D. P., Gajurel, A. P., Bhattarai, R. R., … Bilham, R. (2016). Himalayan strain reservoir inferred from limited afterslip following the Gorkha earthquake. *Nature Geoscience*, 9(7), 533– 537.

Molnar, P., & Chen, W. P. (1983). Focal depths and fault plane solutions of earthquakes under the Tibetan Plateau. *Journal of Geophysical Research*, 88(B2), 1180– 1196.

Monsalve, G., Sheehan, A., Schulte-Pelkum, V., Rajaure, S., Pandey, M., & Wu, F. (2006). Seismicity and one-dimensional velocity structure of the Himalayan collision zone: Earthquakes in the crust and upper mantle. *Journal of Geophysical Research*, 111, B10301. https://doi.org/10.1029/2005JB004062

Nábělek, J., Hetényi, G., Vergne, J., Sapkota, S., Kae, B., Jiang, M., … Hi-CLIMB Team, Hi-CLIMB Team (2009). Underplating in the Himalaya-Tibet collision zone revealed by the Hi-CLIMB experiment. *Science*, 325(5,946), 1371– 1374.

Okada, B. Y. Y. (1992). Internal deformation due to shear and tensile faults in a half-space. *Bulletin of the Seismological Society of America*, 82(2), 1018– 1040.

Ozawa, S. (2011). Coseismic and postseismic slip of the 2011 magnitude-9 Tohoku-Oki earthquake. *Nature*, 475(7,356), 373– 376.

Peltzer, G., Rosen, P., Rogez, F., & Hudnut, K. (1996). Postseismic rebound in fault step-overs caused by pore fluid flow. *Science*, 273(5,279), 1202– 1204.

Peltzer, G., Rosen, P., Rogez, F., & Hudnut, K. (1998). Poroelastic rebound along the Landers 1992 earthquake surface rupture. *Journal of Geophysical Research*, 103(B12), 30,131– 30,145.

Perfettini, H., & Avouac, J.-P. (2007). Modeling afterslip and aftershocks following the 1992 Landers earthquake. *Journal of Geophysical Research*, 112, B07409. https://doi.org/10.1029/2006JB004399

Pollitz, F. F. (2003). Transient rheology of the uppermost mantle beneath the Mojave Desert, California. *Earth and Planetary Science Letters*, 215(1), 89– 104.

Pollitz, F. F. (2014). Post-earthquake relaxation using a spectral element method: 2.5-D case. *Geophysical Journal International*, 198(1), 308– 326. https://doi.org/10.1093/gji/ggu114

Pollitz, F. F. (2015). Post earthquake relaxation evidence for laterally variable viscoelastic structure and water content in the southern California mantle. *Journal of Geophysical Research: Solid Earth*, 120, 2672– 2696. https://doi.org/10.1002/2014JB011603

Pollitz, F. F., Wicks, C., & Thatcher, W. (2001). Mantle flow beneath a continental strike-slip fault: postseismic deformation after the 1999 Hector Mine earthquake. *Science*, 293(5,536), 1814– 1818. https://doi.org/10.1126/science.1061361

Qiu, Q., Hill, E. M., Barbot, S., Hubbard, J., Feng, W. P., Lindsey, E. O., ... Tapponnier, P. (2016). The mechanism of partial rupture of a locked megathrust: The role of fault morphology. *Geology*, 44, 875– 878.

Rousset, B., Barbot, S., Avouac, J.-P., & Hsu, Y.-J. (2012). Postseismic deformation following the 1999 Chi-Chi earthquake, Taiwan: Implication for lower-crust rheology. *Journal of Geophysical Research*, 117, B12405. https://doi.org/10.1029/2012JB009571

Royden, L. H., Burchfiel, B. C., King, R. W., Wang, E., Chen, Z., Shen, F., & Liu, Y. (1997). Surface deformation and lower crustal flow in eastern Tibet. *Science*, 276(5,313), 788– 790.

Ryder, I., Parsons, B., Wright, T. J., & Funning, G. J. (2007). Post-seismic motion following the 1997 Manyi (Tibet) earthquake: InSAR observations and modelling. *Geophysical Journal International*, 169(3), 1009– 1027. https://doi.org/10.1111/j.1365-246X.2006.03312.x

Ryder, I., Bürgmann, R., & Sun, J. (2010). Tandem afterslip on connected fault planes following the 2008 Nima-Gaize (Tibet) earthquake. *Journal of Geophysical Research*, 115, B03404. https://doi.org/10.1029/2009JB006423

Ryder, I., Bürgmann, R., & Pollitz, F. (2011). Lower crustal relaxation beneath the Tibetan Plateau and Qaidam Basin following the 2001 Kokoxili earthquake. *Geophysical Journal International*, 187(2), 613– 630. https://doi.org/10.1111/j.1365-246X.2011.05179.x

Ryder, I., Wang, H., Bie, L., & Rietbrock, A. (2014). Geodetic imaging of late postseismic lower crustal flow in Tibet. *Earth and Planetary Science Letters*, 404, 136– 143.

Savage, J. C., Svarc, J. L., & Yu, S. (2007). Postseismic relaxation and aftershocks. *Journal of Geophysical Research*, 112, B06406. https://doi.org/10.1029/2006JB004584

Scholz, C. H. (1998). Earthquakes and friction laws. *Nature*, 391(1), 37– 42.

Shen, Z.-K., Jackson, D. D., & Ge, B. X. (1996). Crustal deformation across and beyond the Los Angeles basin from geodetic measurements. *Journal of Geophysical Research*, 101(B12), 27,957. https://doi.org/10.1029/96JB02544

Shi, X., Kirby, E., Furlong, K. P., Meng, K., Robinson, R., & Wang, E. (2015). Crustal strength in central Tibet determined from Holocene shoreline deflection around Siling Co. *Earth and Planetary Science Letters*, 423, 145–154. https://doi.org/10.1016/j.epsl.2015.05.002

Sreejith, K., Sunil, P., Agrawal, R., Saji, A. P., Ramesh, D., & Rajawat, A. (2016). Coseismic and early postseismic deformation due to the 25 April 2015, M_w7.8 Gorkha, Nepal, earthquake from InSAR and GPS measurements. *Geophysical Research Letters*, 43(7), 3160– 3168.

Stark, P. B., & Parker, R. L. (1995). Bounded-variable least-squares: An algorithm and applications. *Computational Statistics*, 10(2), 129– 141.

Stevens, V. L., & Avouac, J.-P. (2015). Interseismic coupling on the Main Himalayan thrust. *Geophysical Research Letters*, 42, 5828– 5837. https://doi.org/10.1002/2015GL064845

Tan, K., Yang, S. M., Qiao, X. J., Xu, C. J., & Wang, Q. (2013). Rupture of ramp-décollement faults in the 2008 Wenchuan earthquake-geodetic evidence for the uplift of the Longmen Shan driven by convergent deformation (in Chinese). *Chinese Journal of Geophysics*, 56(5), 1506– 1516. https://doi.org/10.6038/cjg20130509

Tan, K., Zhao, B., Zhang, C., Du RL, W. Q., Huang, Y., ... Qiao, X. J. (2016). Rupture models of the Nepal M_w7.9 earthquake and M_w7.3 aftershock constrained by GPS and InSAR coseismic deformations (in Chinese). *Chinese Journal of Geophysics*, 59(6), 2080– 2093. https://doi.org/10.6038/cjg20160614

Taylor, M., & Yin, A. (2009). Active structures of the Himalayan-Tibetan orogen and their relationships to earthquake distribution, contemporary strain field, and Cenozoic volcanism. *Geosphere*, 5(3), 199– 214. https://doi.org/10.1130/GES00217.1

Thatcher, W. (1983). Nonlinear strain buildup and the earthquake cycle. *Journal of Geophysical Research*, 88, 5893– 5902.

Thomas, A. L. (1993). Poly3d: A three-dimensional, polygonal element, displacement discontinuity boundary element computer program with applications to fractures, faults, and cavities in the earth's crust, Ph.D. thesis, Stanford University.

Unsworth, M., Jones, A. G., Wei, W., Marquis, G., Gokarn, S., Spratt, J., … INDEPTH-MT team, INDEPTH-MT team (2005). Crustal rheology of the Himalaya and southern Tibet inferred from magnetotelluric data. *Nature*, 438(7,064), 78– 81.

van Dam, T., Wahr, J., & Lavallée, D. (2007). A comparison of annual vertical crustal displacements from GPS and Gravity Recovery and Climate Experiment (GRACE) over Europe. *Journal of Geophysical Research*, 112(B3), B03404. https://doi.org/10.1029/2006JB004335

Villegas-Lanza, J. C., Nocquet, J. M., Rolandone, F., Vallée, M., Tavera, H., Bondoux, F., & Chlieh, M. (2016). A mixed seismic-aseismic stress release episode in the Andean subduction zone. *Nature Geoscience*, 9(2), 150– 154.

Wang, K., & Fialko, Y. (2014). Space geodetic observations and models of postseismic deformation due to the 2005 *M*7. 6 Kashmir (Pakistan) earthquake. *Journal of Geophysical Research: Solid Earth*, 119, 7306– 7318. https://doi.org/10.1002/2014JB011122

Wang, K., & Fialko, Y. (2015). Slip model of the 2015 M_w7.8 Gorkha (Nepal) earthquake from inversions of ALOS-2 and GPS data. *Geophysical Research Letters*, 42, 7452– 7458. https://doi.org/10.1002/2015GL065201

Wang, R., & Kümpel, H.-J. (2003). Poroelasticity: Efficient modeling of strongly coupled, slow deformation processes in a multilayered half-space. *Geophysics*, 68(2), 705– 717.

Wen, Y., Li, Z., Xu, C., Ryder, I., & Bürgmann, R. (2012). Postseismic motion after the 2001 M_w7.8 Kokoxili earthquake in Tibet observed by InSAR time series. *Journal of Geophysical Research*, 117, B08405. https://doi.org/10.1029/2011JB009043

Whipple, K. X., Shirzaei, M., Hodges, K. V., & Arrowsmith, J. R. (2016). Active shortening within the Himalayan orogenic wedge implied by the 2015 Gorkha earthquake. *Nature Geoscience*, 9(9), 711– 716.

Wimpenny, S., Copley, A., & Ingleby, T. (2017). Fault mechanics and post-seismic deformation at Bam, SE Iran. *Geophiscial Journal Internaitonal*, 209, 1018– 1035. https://doi.org/10.1093/gji/ggx065

Yamagiwa, S., Miyazaki, S., Hirahara, K., & Fukahata, Y. (2015). Afterslip and viscoelastic relaxation following the 2011 Tohoku-Oki earthquake (M_w9.0) inferred from inland GPS and seafloor GPS/acoustic data. *Geophysical Research Letters*, 42, 66– 73. https://doi.org/10.1002/2014GL061735

Yamasaki, T., & Houseman, G. A. (2012). The crustal viscosity gradient measured from post-seismic deformation: A case study of the 1997 Manyi (Tibet) earthquake. *Earth and Planetary Science Letters*, 351–352, 105– 114.

Zhao, B., Du, R., Zhang, R., Tan, K., Qiao, X., Huang, Y., & Zhang, C. (2015). Co-seismic displacements associated with the 2015 Nepal M_w7.9 earthquake and M_w7.3 aftershock constrained by Global Positioning System

measurements (in Chinese). *Chinese Science Bulletin*, 60(28–29), 2758–2764. https://doi.org/10.1360/N972015-00519

Zhao, B., Huang, Y., Zhang, C., Wang, W., Tan, K., & Du, R. (2015). Crustal deformation on the Chinese mainland during 1998–2014 based on GPS data. *Geodesy and Geodynamics*, 6, 7– 15. https://doi.org/10.1016/j.geog.2014.12.006

Zhou, H.-W., & Murphy, M. A. (2005). Tomographic evidence for wholesale underthrusting of India beneath the entire Tibetan Plateau. *Journal of Asian Earth Sciences*, 25(3), 445– 457.